9 Jet, E_T^{miss}, and mass reconstruction

In this chapter, the reconstruction of the physics quantities relevant to the overall calorimetry is reviewed. There are three main sections. The measurement of jets is discussed in Section 9.1: experimental aspects of jet energy reconstruction and performance of various jet finding algorithms are reviewed, low-p_T jet measurements and forward jet tagging are discussed, finally the special case of τ-jet identification and measurement is studied. Section 9.2 describes the measurement of missing transverse energy. Finally, in Section 9.3, the reconstruction of the mass of objects decaying to jets is discussed: the cases considered include light quark jets, $b\bar{b}$ and $\tau\tau$ jet final states.

9.1 Jet measurement

Jets will be widely used in the analysis of many physics channels at the LHC. Various factors play a role in the chain that goes from the initial parton produced in the hard-scattering process to the reconstructed jet in the calorimeter. Physics effects such as fragmentation, initial and final state radiation, and the co-existence of the underlying event or additional minimum-bias events are intrinsic properties of the events. Detector effects, on the other hand, such as different calorimeter response to charged and neutral hadrons, non-linearities, magnetic field, effects of dead material, cracks between calorimeters, longitudinal leakage, lateral shower size and granularity, and electronic noise, relate to the performance of the detector, which can be optimised.

In the study of physics channels, jets are used in many different ways, for example: in the reconstruction of resonances such as $W \rightarrow jj$, $Z \rightarrow b\bar{b}$ or $t \rightarrow bW$, in measuring jet multiplicity and total jet energy in SUSY searches, for jet vetoes in the central region down to low-p_T's of ~15 GeV for background rejection, for jet tagging in the forward region, and in QCD studies. Specific physics analyses may put emphasis on different requirements such as controlling the energy scale rather than achieving the best efficiency or the best resolution. Minimum-bias events at high luminosity will restrict the area of the calorimeter over which the jet energy can be integrated, hence the optimum 'cone' size will be different for different luminosity conditions. Physics effects such as final state radiation or colour recombination in fragmentation are channel dependent. Hence, there is no unique optimum strategy for jet reconstruction, and the efficiency and calibration will depend on the algorithm, the level of minimum-bias events and the physics channel. In this chapter, the different ingredients to the problem are reviewed in order to disentangle the detector effects from the physics effects. Section 9.1.1 reviews the detector aspects of jet energy reconstruction: calorimeter response, effect of dead material or 'cracks' using a classical 'cone' algorithm as well as the determination of the jet energy. Section 9.1.2 introduces various jet algorithms and discusses some of their basic properties. Section 9.1.3 treats the question of low-p_T jet reconstruction and Section 9.1.4 of forward jet tagging. Section 9.1.5 reviews all the aspects of τ-jet reconstruction and identification. The question of the absolute jet energy scale calibration is treated more specifically in Section 12.5.1.

9.1.1 Experimental aspects of jet energy reconstruction

In this section, aspects of jet reconstruction related to detector performance are reviewed. The sample of jets used are back-to-back $q\bar{q}$ di-jet events generated with PYTHIA 5.7 / JETSET 7.4. The energy deposited in the sensitive parts of the various calorimeter compartments is first converted to total energy using the electromagnetic (EM) scale. The various calorimeters have different degrees of non-compensation and hence a different response to the charged hadrons jet component. Any reconstruction algorithm will have to apply additional weights to take that effect into account. In addition, the energy loss as a function of η is different for the neutral and charged hadron components of the jets (see Figure 5-25). The energy loss for jets is shown in Figure 9-1. Due to the width of the jets, the impact of the dead material in the vertical crack at $|\eta| \approx 1$ and of the corners of the cryostat walls at $|\eta| \approx 1.45$ are merged and affect a broader region than in the case of single particles (see Figure 5-25).

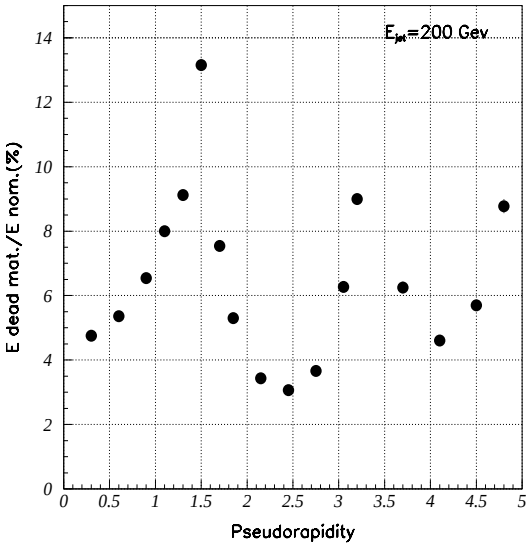

Figure 9-1 Fractional energy loss of 200 GeV jets in dead material as a function of pseudorapidity.

9.1.1.1 Performance for jet energy reconstruction with the 'Benchmark procedure'

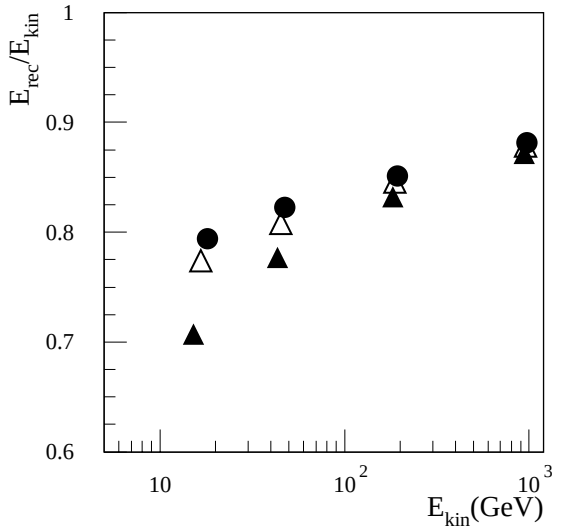

Figure 9-2 Average ratio of the reconstructed jet energy E_{rec} over the particle level jet energy E_{kin} as a function of E_{kin} for di-jet events at $|\eta| = 0.3$ for three cone sizes $\Delta R = 0.4$ (black triangles), $\Delta R = 0.7$ (open triangles) and $\Delta R = 1.5$ (black dots). The calorimeters are calibrated at the EM scale. No correction for energy loss in the dead material is applied.

In the 'Benchmark procedure' for jet energy reconstruction, a standard fixed-cone jet algorithm is applied. Transverse energies in towers are projected in a matrix of (0.1×0.1) granularity in ($\Delta\eta \times \Delta\phi$) with tower energies calibrated at the EM scale. The highest E_T tower, above a cut, is selected as a jet seed and a cone is created, centred on the seed. Two cone sizes have been considered: $\Delta R = 0.4$ and $\Delta R = 0.7$. In order to disentangle the effect of fragmentation and of calorimeter response, the reconstructed energy in the calorimeter inside the cone (E_{rec}) is normalised to the sum of the momenta of the generated particles inside the cone (E_{kin}), taking into account the effect of the magnetic field. Figure 9-2 shows an example of the mean ratio of (E_{rec}/E_{kin}). No correction for energy loss in the dead material is applied. This ratio is typically of the order of 0.8 and varies as a function of the parton energy and the cone size. This results from the fact that the energy spectrum of the particles contained in the cone depends on the parton energy, and the

e/π ratio varies with the hadron energy. Out-of-cone losses due to lateral hadronic shower size are larger for a smaller cone. A procedure that minimises $\sum(E_{rec}-E_{kin})^2+\beta\times\sum(E_{rec}-E_{kin})$ is then applied to adjust the calibration coefficients for each parton energy and for each cone size. This 'Benchmark procedure' includes weights for each calorimeter compartment, the presampler, the EM and hadronic calorimeters. Correction terms for the energy loss in the dead material between the EM and hadronic compartments of the central barrel and extended barrels are added. Special weights for the two intermediate tile calorimeters in the vertical gaps and the scintillators covering part of the end-cap cryostat front wall are adjusted to compensate for the energy loss in the dead material located in the cracks (see Section 5.3.2.1 and Figure 5-i) [9-1][9-2][9-3].

Energy scan

Jet energy scans were performed at various values of pseudorapidity. The coefficients used in the jet energy reconstruction algorithm were fitted at every energy point (see Section 9.1.1.2 for a discussion of their energy dependence). In the central region, the range of energies considered was 20 GeV to 1 TeV, while in the end-cap region, the energies relevant for the physics start at about 100 GeV. No electronic noise or pile-up was included at this level. The performance of the barrel and end-cap calorimeters are shown in Figure 9-3 and Figure 9-4, respectively.

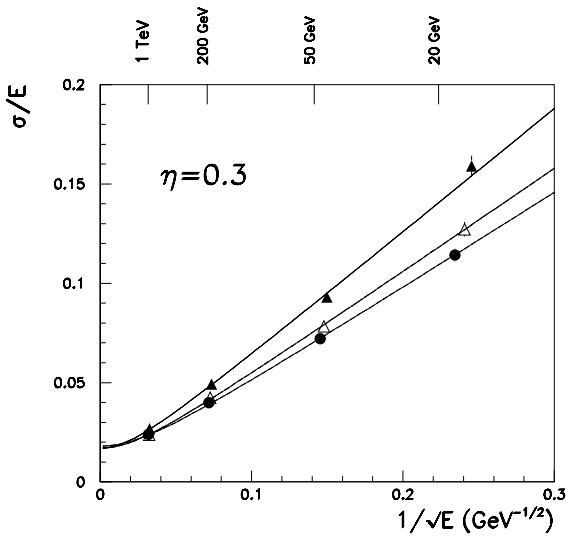

Figure 9-3 Energy resolution in the range from 20 GeV to 1 TeV at $|\eta| = 0.3$. Black circles are obtained using energies summed in cone size of $\Delta R = 1.5$; open triangles for cone size $\Delta R = 0.7$ and black triangles for cone size $\Delta R = 0.4$.

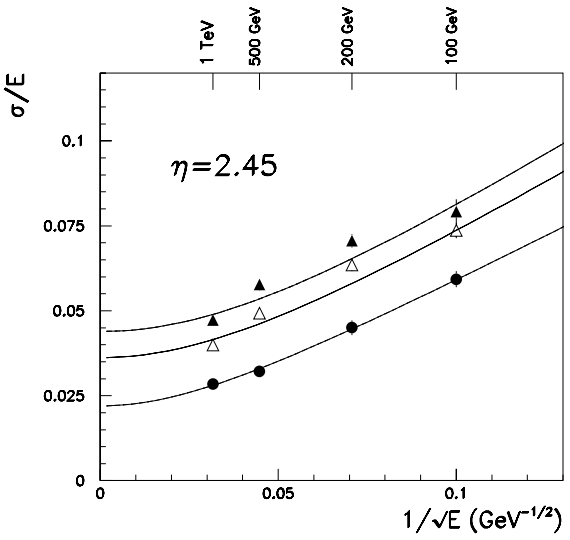

Figure 9-4 Energy resolution in the range 100 GeV to 1 TeV at $|\eta| = 2.45$. Black circles are obtained using the total energy in the calorimeter; open triangles for cone size $\Delta R = 0.7$ and black triangles for cone size $\Delta R = 0.4$.

The results are shown for the total sum of energies in the calorimeter and for two cone sizes $\Delta R = 0.7$ and $\Delta R = 0.4$. The resolution was fitted with the expression $\sigma/E = a/\sqrt{E} \oplus b$. As the cone size becomes smaller, there is a deterioration of the resolution. In the barrel region, the effect is confined to the sampling term which suffers from the fluctuations of the out-of-cone losses from the fragmentation and magnetic field effects. The high energy jets are only slightly affected, since, due the boost, the particles in the jet are more collimated and well contained in

Table 9-1 Coefficients of the jet energy resolution fitted by the expression $\sigma/E = a/\sqrt{E} \oplus b$.

	Barrel region η=0.3		End-cap region η=2.45	
	a (%GeV$^{1/2}$)	**b (%)**	**a (%GeV$^{1/2}$)**	**b (%)**
Full calorimeter	48.2 ± 0.9	1.8 ± 0.1	55.0 ± 2.5	2.2 ± 0.2
Cone ΔR=0.7	52.3 ± 1.1	1.7 ± 0.1	64.2 ± 2.4	3.6 ± 0.2
Cone ΔR=0.4	62.4 ± 1.4	1.7 ± 0.2	68.4 ± 3.4	4.4 ± 0.2

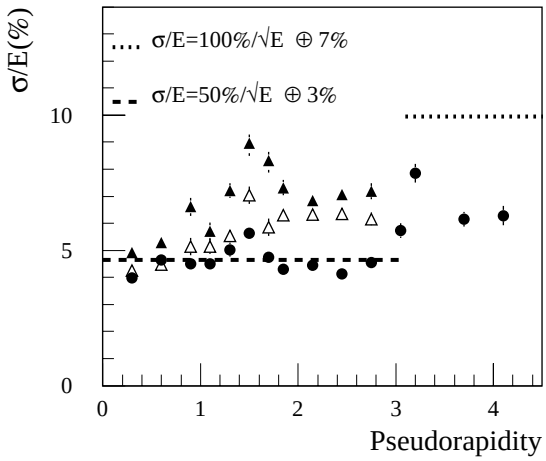

Figure 9-5 Energy resolution for jets of constant energy (200 GeV) across the full pseudorapidity coverage of the calorimeter. Black dots are for total energy in the calorimeter; open triangles for cone size ΔR = 0.7 and black triangles for cone size ΔR = 0.4.

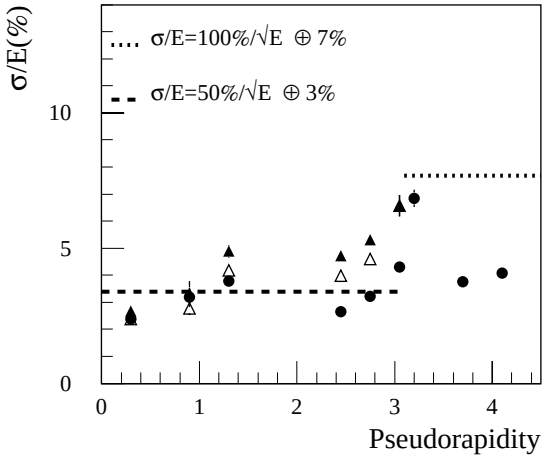

Figure 9-6 Energy resolution for jets of constant energy (1 TeV) across the full pseudorapidity coverage of the calorimeter. Black dots are for total energy in the calorimeter; open triangles for cone size ΔR = 0.7 and black triangles for cone size ΔR = 0.4. Jets of 1 TeV have been simulated at fewer pseudorapidity values than 200 GeV jets.

the cone. In the end-cap, at $|\eta| = 2.45$, both the statistical and the constant terms are affected, because the hadronic shower size becomes non-negligible with respect to the cone size and energy is lost out of the cone even for high-energy jets.

Scan across pseudorapidity

As shown in Figure 9-1, there are non-uniformities in the calorimeter. In the transition region between the barrel and the end-cap, the larger amount of dead material affects jets with pseudorapidity from 1.0 to about 1.8. In the transition region between the end-cap and the forward calorimeters, the region affected extends roughly from $|\eta| = 3.0$ to 3.5. Scans across pseudorapidity were carried out with jets of various energies. Figure 9-5 shows the resolution obtained for jets with a constant energy of 200 GeV, and Figure 9-6 for 1 TeV jets. Values are compared to the target resolution of $\sigma/E = 50\%/\sqrt{E} \oplus 3\%$ for precision jet energy measurement in the central pseudorapidity region, and the target resolution of $\sigma/E = 100\%/\sqrt{E} \oplus 7\%$ for jet tagging and $E_{\mathrm{T}}^{\mathrm{miss}}$ measurements in the forward region. Only a relatively small deterioration of the resolution is observed in the crack region around $|\eta| = 1.5$ when the total energy in the calorimeter is used. The effect is more pronounced when a cone algorithm is applied. The deterioration of

the resolution is also observed in the transition region between the end-cap and the forward calorimeters. In the FCAL region, the resolution is shown only for the total energy in the calorimeter, a more detailed discussion of the reconstruction of jets in the FCAL is given in Section 9.1.4.

The energy dependence of the resolution has been fitted at various points in pseudorapidity with the parametrisation $\sigma/E = a/\sqrt{E} \oplus b$. The resulting statistical term a and constant term b are shown in Figure 9-7 and Figure 9-8. When all calorimeter energy is summed, the constant term deteriorates from 2% to about 3.5% in the crack region around $|\eta| = 1.5$ and increases to 4% as one approaches $|\eta| = 3.2$. In the central region out-of-cone losses due to fluctuations in the fragmentation affect mostly lower energy jets and thus only the statistical term. More energetic jets have more collimated fragmentation products and their corresponding hadronic shower is well contained. But as the pseudorapidity increases, a cone of constant size in $(\Delta\eta \times \Delta\phi)$ decreases in terms of the solid angle sustained. Therefore the hadronic shower size becomes increasingly larger with respect to the cone size. Losses due to hadronic shower leakage affect the more energetic jets, resulting in an increase of the constant term.

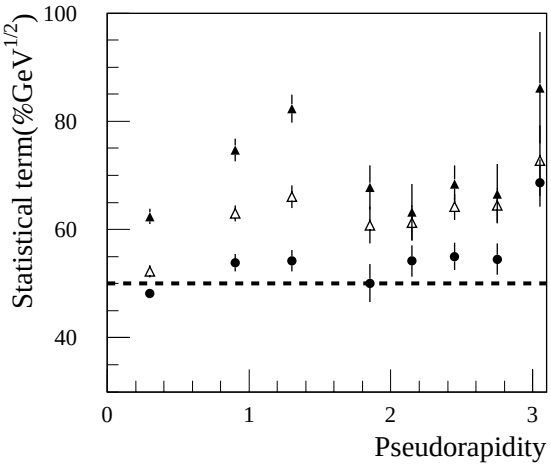

Figure 9-7 Statistical term of the fitted energy resolution for jets as a function of pseudorapidity. Black dots are for total energy in the calorimeter, open triangles for cone size $\Delta R = 0.7$ and black triangles for cone size $\Delta R = 0.4$.

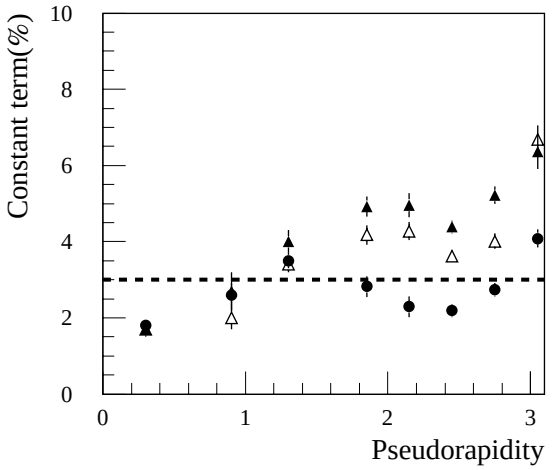

Figure 9-8 Constant term of the fitted energy resolution for jets as a function of pseudorapidity. Black dots are for total energy in the calorimeter, open triangles for cone size $\Delta R = 0.7$ and black triangles for cone size $\Delta R = 0.4$.

Effect of electronic noise and pile-up

The effect of electronic noise was studied in the barrel region at $|\eta| = 0.3$. The noise was simulated applying the digital filtering method. The rms of the noise is of the order of 200 MeV per tower of 0.1×0.1 in $\Delta\eta \times \Delta\phi$, a value estimated for the calorimeter calibrated at the EM scale (Chapter 5). The noise contribution in cones of $\Delta R = 0.4$ and $\Delta R = 0.7$ is 1.4 GeV and 2.5 GeV, respectively. When the jet energy was reconstructed, additional factors were applied to correct for the effect of the non-compensation. Figure 9-2 shows that these factors are of the order of 1.25. The level of noise at the 'hadronic' scale is then equivalent to 1.9 and 3.3 GeV for cone sizes $\Delta R = 0.4$ and $\Delta R = 0.7$, respectively. The data were fitted by the expression $\sigma/E = a/\sqrt{E} \oplus b \oplus c/E$.

The results are given in Table 9-2 and shown in Figure 9-9 for the two cone sizes. The statistical term *a* and noise term *c* are correlated and there are only four energy points available, hence they have large errors. The procedure used was to keep the statistical term *a* and constant term *b* fixed at the values obtained when no electronic noise was added, and, to fit only the noise term *c*. When no cell cut was applied, the noise term found was in good agreement with the estimated contribution. Compatible values were obtained when the three coefficients were fitted simultaneously. Different cell cuts were used and the corresponding noise evaluated. Symmetric thresholds were applied to minimise the bias induced on energy. The scan was done between zero and three times the rms of the noise by steps of 0.5. The optimal cut depends on the energy of the jet and the cone size. The best overall performance was obtained for a 2.5σ cut. The noise contribution was then reduced, the main improvement being found for a cone size $\Delta R = 0.7$ where the noise term decreases from 3 to 2 GeV. The resolution obtained for the two cone sizes, once the electronic noise contribution is included, are similar.

Table 9-2 Coefficients of the jet energy resolution fitted by $\sigma/E = a/\sqrt{E} \oplus b \oplus c/E$ when electronic noise is included. The coefficients *a* and *b* are fixed to the values obtained without noise.

cell cut	a (%GeV$^{1/2}$)	b(%)	c (GeV)
no cut $\Delta R = 0.7$	52.3	1.7	3.0 ± 0.1
2.5σ $\Delta R = 0.7$	52.3	1.7	2.0 ± 0.1
no cut $\Delta R = 0.4$	62.4	1.7	2.0 ± 0.1
2.5σ $\Delta R = 0.4$	62.4	1.7	1.7 ± 0.2

The effect of the pile-up from minimum-bias events was studied in the barrel region at $|\eta| = 0.3$. In addition to the pile-up, electronic noise was added without applying digital filtering (see Section 4.2.4). The contribution of the pile-up and noise in a tower of 0.1×0.1 in $\Delta\eta\times\Delta\phi$ is slightly asymmetric. The mean value is 50 MeV and the rms about 0.5 GeV. In a cone of $\Delta R = 0.4$ ($\Delta R = 0.7$), the pile-up contributes 3.5 GeV (11 GeV). Once the jets are calibrated to the 'hadronic' scale, the equivalent noise term is 4.7 GeV (14 GeV). The resolution obtained for jets reconstructed with cone size $\Delta R = 0.4$ are given in table Table 9-3 and Figure 9-10. No E_T tower cut, nor cell energy cut, were applied to the data.

Table 9-3 Terms of the jet energy resolution fitted by $\sigma/E = a/\sqrt{E} \oplus b \oplus c/E$ when pile-up and electronic noise are included. First row: *a* and *b* fixed to the values obtained without electronic noise. Second row: only *b* fixed to that value.

a (%GeV$^{1/2}$)	b(%)	c (GeV)
62.4 fixed	1.7 fixed	4.7 ± 0.2
81.3 ± 2.9	1.7 fixed	3.9 ± 0.3

9.1.1.2 Determination of the jet energy

In beam tests, several algorithms for reconstructing the energy of pions have been applied [9-4][9-5][9-6][9-7]. The performance of two of them for the determination of the jet energy are presented in this section [9-8]. The algorithms are the Sampling-dependent weighting technique [9-4] with weights applied to the different calorimeter compartments, and the H1 based approach with weights applied directly to the cell energies [9-9]. The data samples used were the fully simulated back-to-back di-jet events with quark energies E_0 equal to 20, 50, 200 and 1000 GeV at $|\eta| = 0.3$, contained in the Barrel Calorimeter. The cell electronic noise contribution to the EM Calorimeter response was simulated applying the digital filtering method. The jets were reconstructed using the fixed-cone jet algorithm [9-10]. The jet seed threshold on the transverse energy in a tower was set to $E_s = 2$ GeV. The cone sizes used in this analysis were $\Delta R = 0.4$ and 0.7. Events in which two, and only two, reconstructed jets have a transverse energy larger than the

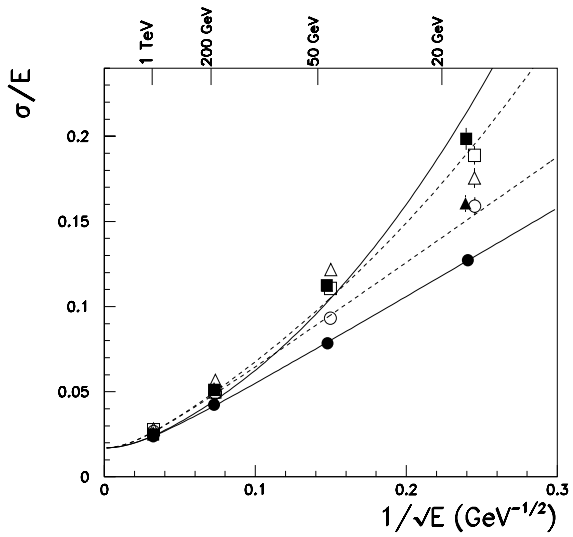

Figure 9-9 Effect of the electronic noise on the jet energy resolution: black dots (open dots) are for cone size $\Delta R = 0.7$ ($\Delta R = 0.4$) when no electronic noise is included; black squares (open squares) are for cone size $\Delta R = 0.7$ ($\Delta R = 0.4$) with electronic noise included; black triangles (open triangles) are for cone size $\Delta R = 0.7$ ($\Delta R = 0.4$) with a cell energy cut at 2.5σ of the noise. The data are fitted with the expression $\sigma/E = a/\sqrt{E} \oplus b \oplus c/E$. The full lines (dashed lines) show the fit to the data with cone $\Delta R = 0.7$ ($\Delta R = 0.4$) without and with noise (no cell cut), see Table 9-2.

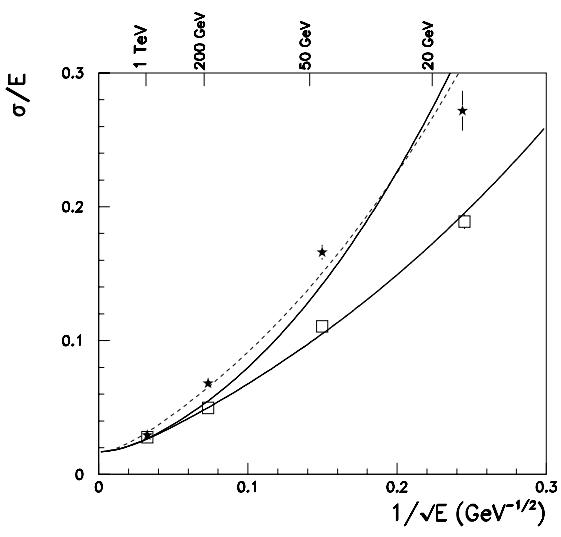

Figure 9-10 Jet energy resolution obtained with electronic noise and pile-up included for cone size $\Delta R = 0.4$: stars are for jets with pile-up and electronic noise, open squares with electronic noise only (digital filtering applied). The data including pile-up are fitted with $\sigma/E = a/\sqrt{E} \oplus b \oplus c/E$. The full lines show the result when a and b are fixed to the values obtained without pile-up or noise and the dashed line when only b is fixed (see Table 9-3).

threshold value $E_T = 5$ GeV for $E_0 = 20$ GeV and $E_T = 20$ GeV for E_0 larger than 20 GeV were retained. To reduce the effect of the electronic noise on the determination of the energy, the absolute values of the cell energies were required to be larger than two times the rms of the electronic noise of the cells and the transverse energy per tower of size 0.1×0.1 in $\Delta\eta\times\Delta\phi$ was required to be larger than 0.2 GeV.

The offline calibration: general procedure

As was shown in the previous section, the ATLAS calorimeters are not compensating and a calibration procedure has to be applied to determine the jet energy and to improve the resolution. In a general form, the reconstructed energy of a jet k can be expressed as a parametric function of the cell energy $\overline{\varepsilon_{i,j}}$ as

$$E^k = \sum_l f(a_l; \overline{\varepsilon_{i,j}}) \qquad 9\text{-}1$$

where i defines the calorimeter sampling to which the cell belongs, j is its position in pseudorapidity, and l runs from one to the total number of parameters used. Here, and in the following, the symbol overline on top of an energy indicates that these values were obtained using the EM scale calibration. For each parton energy, the values of the parameters a_l minimise the quantity

$$\sum_{k=1}^{K} (E^k - E^k_{kin})^2 + \beta \sum_{k=1}^{K} (E^k - E^k_{kin}) \qquad 9\text{-}2$$

This function is minimised simultaneously with respect to the Lagrange multiplier β that forces the reconstructed energy in the cone to reproduce the reference energy E^k_{kin}, the particle level energy inside the cone. In the real experiment, the particle level energy of a jet is unknown. Therefore the parameters a_l were parametrised in turn as a function of E_{kin} using smooth functions

$$a_l = g_l(b_n; E_{kin}) . \qquad 9\text{-}3$$

The values of the parameters b_n were determined by fitting Equation 9-3 to the values a_l obtained using the knowledge of the energy of the particles associated with the jet. The correlations between the parameters were not taken into account. The following iteration procedure was then applied: *a*) define a starting value for the reconstructed energy, here the value obtained applying the EM scale calibration was used; *b*) determine the parameters a_l using Equation 9-3 and reconstruct the energy using Equation 9-1; *c*) recompute the weights using the energy reconstructed in *b*); *d*) iterate the procedure until the change in the energy is smaller than 1 MeV. Typically, less than ten iterations are needed.

First example of the offline calibration: the Sampling method

The energy of the jet *k*, E^k, is expressed as a linear combination of the energies $\overline{E^k_i}$ deposited in the presampler, in the EM Calorimeter, and in the Hadronic Tile Calorimeter (i = 1, 2 and 3 respectively):

$$E^k = a_1\overline{E^k_1} + a_2\overline{E^k_2} + a_3\overline{E^k_3} + a_4\overline{E^k_4} .$$

The fourth term in the equation describes the deposited energy in the cryostat. The quantity $\overline{E^k_4}$ was parametrised according to :

$$\overline{E^k_4} = \sqrt{\overline{E^k_{em3}} \cdot \overline{E^k_{had1}}},$$

where $\overline{E^k_{em3}}$ and $\overline{E^k_{had1}}$ are the electromagnetic scale energies deposited in the third compartment ('sampling') of the EM Calorimeter and in the first compartment of the Hadronic Tile Calorimeter respectively. This is the 'Benchmark method' applied in the previous section. Using eight parameters instead of four, that is one for each longitudinal calorimeter compartment plus the cryostat term, did not improve the results significantly; therefore, the simpler approach was selected.

Second example of the offline calibration: the H1 method

The H1 method is based on the study of the energy deposited by the particles of the jet in the individual cells of the calorimeters. The parametrisation chosen for the reconstructed energy of a jet inside the cone was

$$E^k = \overline{E^k_1} + \sum_j \alpha_2(\overline{\varepsilon_{2,j}}) \times \overline{\varepsilon_{2,j}} + \sum_j \alpha_3(\overline{\varepsilon_{3,j}}) \times \overline{\varepsilon_{3,j}} + \alpha_4\overline{E^k_4} \qquad 9\text{-}4$$

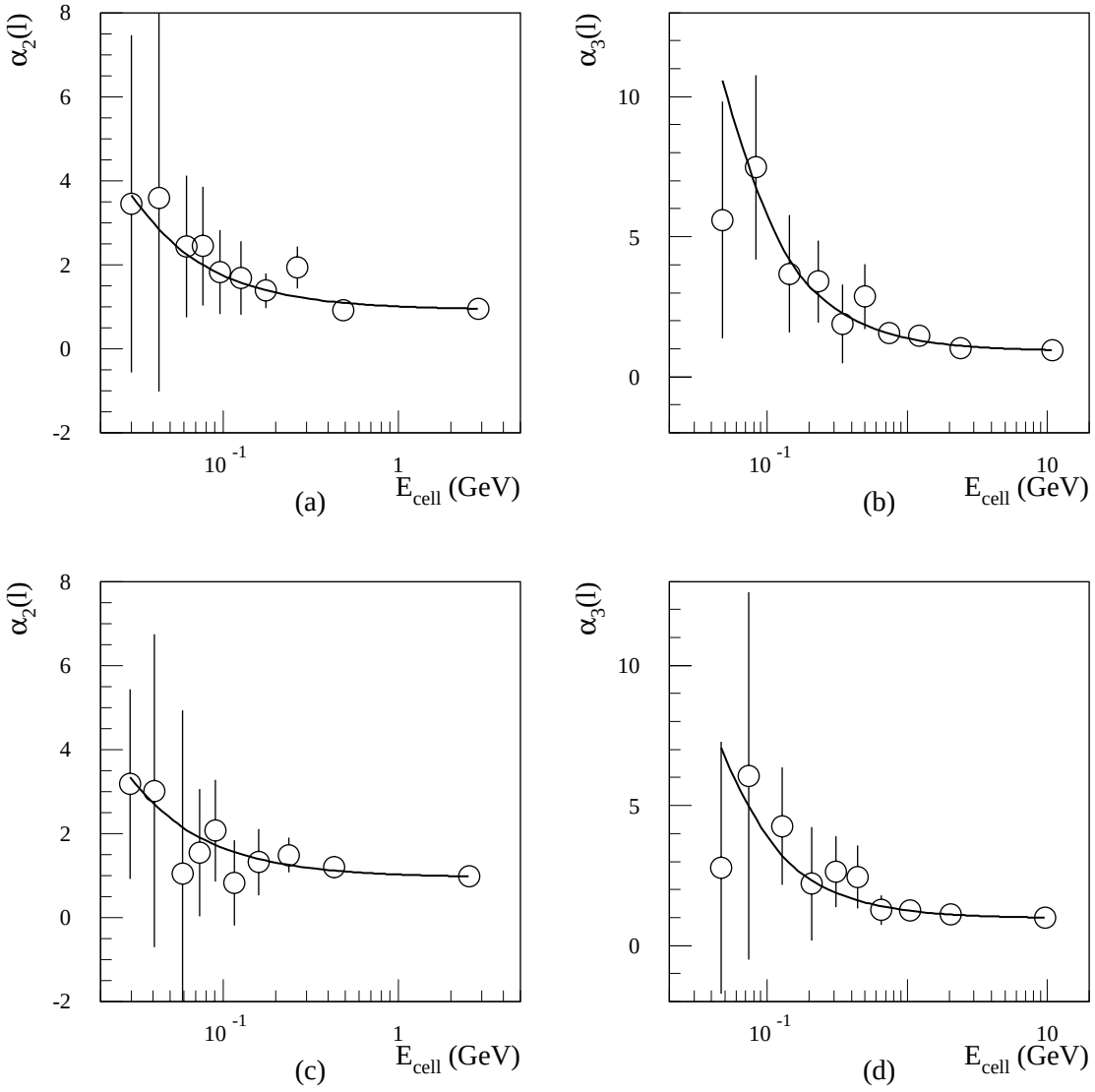

Figure 9-11 H1 method: dependence of the parameters $\alpha_i(l)$ (i = 2, 3) on the cell energy for E_0 = 200 GeV, a) EM Calorimeter with ΔR = 0.4, b) Hadronic Tile Calorimeter with ΔR = 0.4, c) EM Calorimeter with ΔR = 0.7, d) Hadronic Tile Calorimeter with ΔR = 0.7.

where the first term is the total energy deposited in the presampler, the second and third terms are the sums of the energies of all the cells in the EM and hadronic calorimeters, and the fourth term is the cryostat correction defined as before. The $\alpha_i(\overline{\varepsilon_{i,j}})$'s are coefficients that multiply the energy in the cells in the EM Calorimeter (α_2) and the hadronic calorimeter (α_3). They are parametrised by functions that depend on two parameters:

$$\alpha_2(\varepsilon) = a_1 + \frac{a_2}{|\varepsilon|},\ \alpha_3(\varepsilon) = a_3 + \frac{a_4}{|\varepsilon|} \text{ and } \alpha_4 = a_5. \qquad 9\text{-}5$$

The response of a cell with a small signal is corrected upwards to make its response equal to that of cells with large (typically electromagnetic) deposited energy. Introducing a parametric function of the same type that multiplies the energy deposited in the presampler cells did not improve the reconstruction of the jet energies significantly and therefore was not used.

To determine the functions $\alpha_i(\overline{\varepsilon_{i,j}})$ of Equation 9-4, the distributions of the energies deposited in the cells belonging to the EM and Hadronic Tile Calorimeters were divided into ten bins of equal statistics. In this case, the functions $\alpha_i(\overline{\varepsilon_{i,j}})$ are represented by two vectors of dimension 10: $\alpha_i(\overline{\varepsilon_{i,j}}) = \alpha_i(l)$ ($i = 2, 3$; $l = 1, 10$), where l defines the interval in the cell energy. The minimisation of Equation 9-2 produced the values of the vectors $\alpha_i(l)$ shown in Figure 9-11. The errors in the figure are the rms values of five independent determinations of the parameters obtained by breaking the data samples at each energy into five separate sets of equal statistics and solving the minimisation equation for each set. The fits of the function given in Equation 9-5 have a good χ^2 and the corresponding curves are also shown. The results obtained for resolution and linearity with the simple parametrisation of Equation 9-5 are very close to the results obtained using ten parameters for each calorimeter.

Parametrisation of the a_l's as a function of the beam energy

As an example, Figure 9-12 shows the parametrisation with the particle level jet energy of the a_l's obtained using the Sampling method. Also the values of the parameters resulting from the fits are shown in the figures. Similar smooth shapes were obtained with the H1 method. The results for resolution and linearity obtained without prior knowledge of the energy, applying an iterative process based on these parametrisations, are very close to the results obtained using the knowledge of E^k_{kin}.

Results

The jet fractional energy resolutions and linearities are given in Table 9-4 and Table 9-5 respectively. All the results were obtained fitting a Gaussian function to the data using the full lineshape. As in the previous section, the jet fractional energy resolution was calculated as the width of the distributions of $E^k - E^k_{kin}$ divided by the mean value of the reconstructed energy. The normalised response is given by $\mu = \langle E^k / E^k_{kin} \rangle$.The H1 method gives better resolutions than the Sampling method. Enlarging the cone size does not improve significantly the energy resolution due to the increase of the electronic noise, except for the low energy 20 GeV point. The residual non-linearities are smaller than 2% and 3% using the H1 and the Sampling method respectively.

Table 9-4 Jet energy resolutions obtained with the Sampling and the H1 methods ($|\eta| = 0.3$).

	Sampling method: σ/E [%]		**H1 method: σ/E [%]**	
E_0 **[GeV]**	ΔR **= 0.4**	ΔR **= 0.7**	ΔR **= 0.4**	ΔR **= 0.7**
20	15.7 ± 0.7	13.7 ± 0.6	14.5 ± 0.7	12.5 ± 0.5
50	10.2 ± 0.3	9.8 ± 0.3	8.5 ± 0.3	8.0 ± 0.2
200	5.3 ± 0.2	4.7 ± 0.1	4.0 ± 0.1	4.0 ± 0.1
1000	2.4 ± 0.1	2.4 ± 0.1	2.2 ± 0.1	2.3 ± 0.1

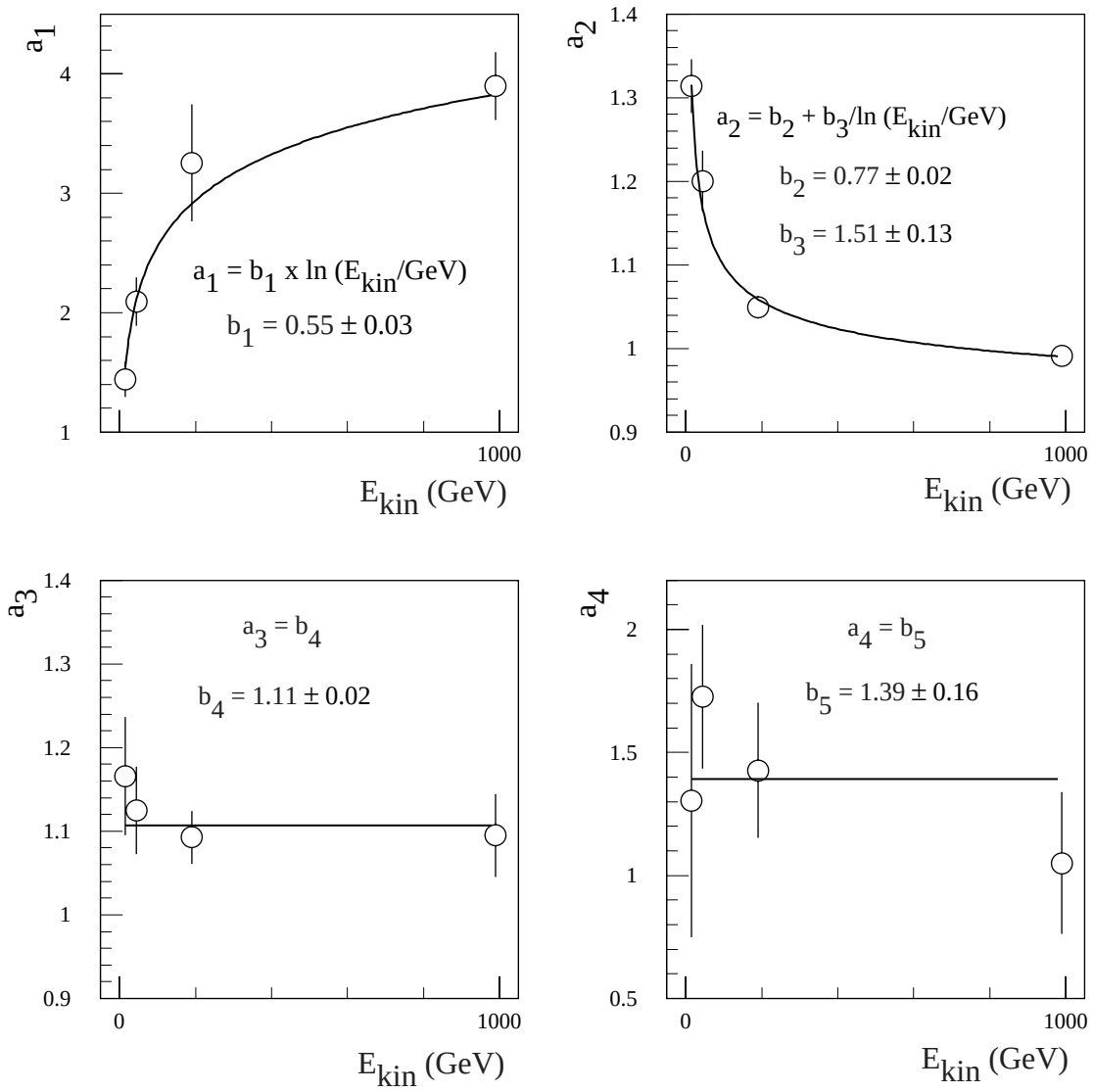

Figure 9-12 parametrisation of the a_i's obtained using the Sampling method with $\Delta R = 0.7$, as a function of the particle level jet energy.

Table 9-5 Residual jet energy non-linearities (see text): (1-μ) in percent (|η| = 0.3).

	Sampling Method		**H1 Method**	
E_0 **[*GeV*]**	ΔR **= 0.4**	ΔR **= 0.7**	ΔR **= 0.4**	ΔR **= 0.7**
20	0.1 ± 0.9	-0.2 ± 0.7	1.1 ± 0.8	2.1 ± 0.6
50	-2.5 ± 0.4	-2.9 ± 0.3	1.3 ± 0.3	-1.5 ± 0.3
200	0.1 ± 0.2	0.2 ± 0.2	-0.3 ± 0.2	-1.4 ± 0.1
1000	2.4 ± 0.2	2.5 ± 0.1	1.7 ± 0.1	2.1 ± 0.1

The energy resolutions have been parametrised according to:

$$\sigma/E = a/\sqrt{E} \oplus b\,.$$

The results obtained for the two cone sizes and the two calibration methods are shown in Figure 9-13 and summarised in Table 9-6. The results obtained with the Sampling method can be compared to the values shown in Figure 9-9 obtained with the 'Benchmark procedure' after applying a 2.5σ symmetric cut on the noise. They show consistent results except for the 20 GeV point which shows a better resolution in this analysis, as a result of the tighter selection cuts applied. The method presented here could be improved by taking into account the correlations existing between the a_l's when parametrising them as a function of the energy.

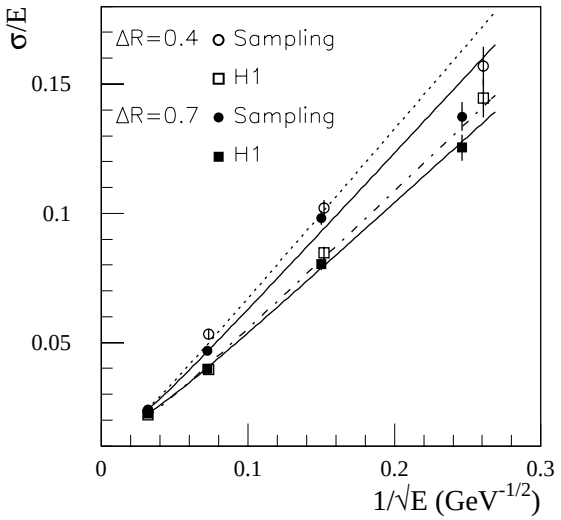

Figure 9-13 Jet energy resolutions obtained with the sampling and H1 methods for the two cone sizes: the full lines represents the fitted resolution for cone size ΔR = 0.7 and the dashed lined for cone size ΔR = 0.4.

In summary, it is found that the jet energy can be determined reliably without prior knowledge of the particle level energy of the jet by using simple smooth functions to describe the energy dependence of the calibration coefficients. The results have been obtained in the central barrel region, at $|\eta|$ = 0.3. A total of five parameters are used for the Sampling method and six for the H1 method. Essentially the same performance for the energy resolution and linearity is obtained as when the particle level jet energy is known. The H1 method gives better performance both in resolution and residual non-linearities.

Table 9-6 Parameter values obtained fitting the energy dependence of the jet energy resolution (|η| = 0.3).

	Sampling Method		**H1 Method**	
	ΔR = 0.4	**ΔR = 0.7**	**ΔR = 0.4**	**ΔR = 0.7**
a (%GeV$^{1/2}$)	66.0 ± 1.5	61.2 ± 1.3	53.9 ± 1.3	51.5 ± 1.1
b (%)	1.2 ± 0.3	1.4 ± 0.2	1.3 ± 0.2	2.5 ± 0.2
χ^2 prob. (%)	1.6	0.8	27.3	66.7

9.1.1.3 High-p_T jet energy calibration

Physics processes involving known processes such as Z+jet events or $W \rightarrow jj$ decays from top events will provide *in situ* jet energy calibration up to about 500 GeV (see Chapter 12). It will be necessary to extrapolate the jet energy calibration up to the highest jet energies that will be reached at the LHC.

A test was made with the parametrisation of the energy dependence of the calibration coefficients discussed in the previous section. The parameters of the energy dependence, the b_n parameters of Equation 9-3, were fitted using the jets produced by 20, 50 and 200 GeV quarks.

Afterwards the 1 TeV jets were reconstructed using the extrapolated coefficients. Using the H1 method with a $\Delta R = 0.7$ cone, the same resolution was obtained and the non-linearity was $(2.9 \pm 0.1)\%$, about 1% more than when the full energy range was fitted.

Since very high-p_T jets will not be available for *in situ* calibration, the extrapolation of the calibration coefficients can only be checked on jets fully simulated by Monte Carlo. In addition to the uncertainties arising from physics effects such as fragmentation and cone size, the response of the calorimeter to hadrons plays a non-negligible role. It was shown in Chapter 5 that the e/π ratio is larger than one and depends on the hadron energy. The ratio is given by the formula

$$e/\pi = \frac{e/h}{1 + (e/h - 1) \cdot F(\pi^0)} \qquad 9\text{-}6$$

The two ingredients of the hadron response are the intrinsic responses to purely electromagnetic energy (e) and purely hadronic energy (h), and the fraction of π^0's produced in the hadron interaction $F(\pi^0)$. For example, in the barrel calorimeter, typical values of e/π from test beam data are 1.25 (1.10) at 20 GeV (300 GeV). A fit to the test-beam data gives a value for e/h of 1.37 ± 0.01,

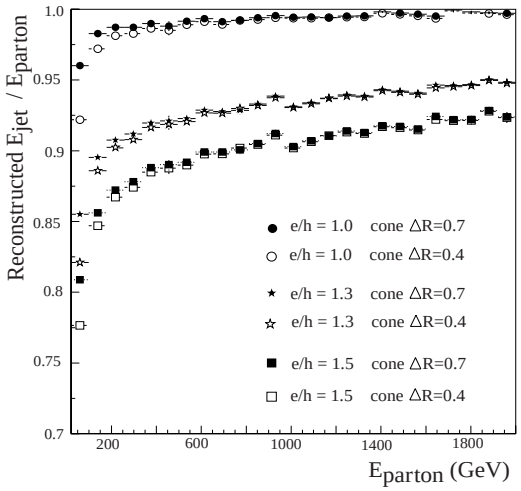

Figure 9-14 Reconstructed jet energy for different levels of non-compensation (e/h = 1.0, 1.3, 1.5) and for two cone sizes (ΔR = 0.7 and 0.4).

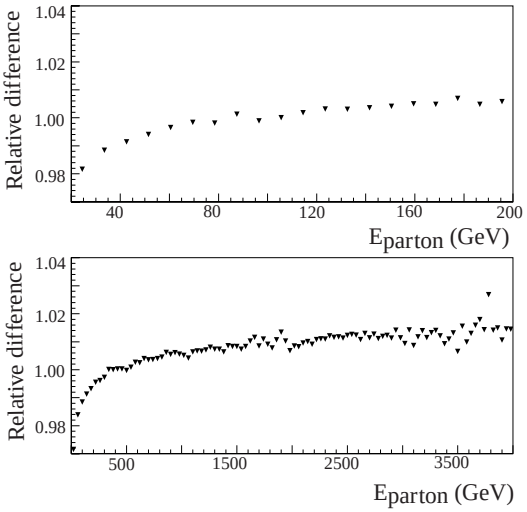

Figure 9-15 Relative difference in the calibration for two degrees of non-compensation (e/h = 1.3, 1.5). In the top plot, the responses are equalised at 100 GeV and in the bottom plot at 500 GeV.

while a fit to data simulated with the G-CALOR Monte Carlo results in 1.31 ± 0.01. Different hadronic shower Monte Carlo packages give different predictions for the degree of non-compensation of the calorimeter, with differences of the order of ±0.2 [9-11]. The failure of the hadronic shower Monte Carlo package to reproduce e/h has been simulated [9-12]. A parametrisation of the hadron response based on Equation 9-6 has been implemented in ATLFAST. The fraction of π^0's in pion and proton induced showers were generated according to the parametrisation given in [9-13]. A sample of QCD di-jet events were generated: one parton was required to be in the central region ($|\eta| < 0.5$) and initial and final state radiation and multiple interactions were not switched on. Figure 9-14 shows the reconstructed jet energy for three values of

e/h: 1.0, 1.3 and 1.5 when the calorimeters were calibrated at the EM scale. At 200 GeV for example, the shift between the parton energy and the reconstructed jet energy is 10% (14%) for e/h = 1.3 (1.5), while at 2 TeV the shift reduces to 6% (8%).

Assuming that *in situ* calibration will provide the absolute jet energy scale at least in part of the energy range, it is interesting to look at the residual differences in non-linearity for different values of *e/h*. Figure 9-15 shows that they are of the order of 2 to 3% below 200 GeV and 2% in the range 200 GeV to 4 TeV. The consequence of such an uncorrected non-linearity was studied in the case of the measurement of the inclusive high-p_T jet cross-section. Since the cross-section falls rapidly with p_T, a mis-calibration generates an apparent disagreement with the QCD prediction. Figure 9-16 shows the ratio of the measured cross-section and the QCD prediction in the range 500 GeV to 4 TeV in the case where the degree of non-compensation *e/h* is overestimated by 0.2, *i.e.* is equal to 1.5 instead of 1.3. See Chapter 15 and Section 21.5 for a more detailed discussion of the implications for the physics.

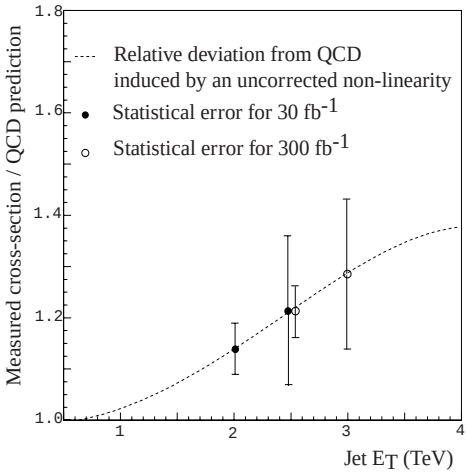

Figure 9-16 Apparent deviation from the QCD cross-section due to the mis-calibration of the calorimeter.

9.1.1.4 Conclusions

The intrinsic calorimeter jet energy resolution is very good across the full pseudorapidity range. The effect of limited cone size in the jet reconstruction on the jet energy resolution increases with pseudorapidity as the hadronic shower size becomes larger. A deterioration of the resolution is observed in the crack regions, the effect being more pronounced when the jet reconstruction is limited to a cone. In the barrel calorimeter, the electronic noise, with digital filtering applied, contributes 3.0 GeV (1.7 GeV) to the jet energy resolution when the jet is reconstructed in a cone of $\Delta R = 0.7$ ($\Delta R = 0.4$). The combined effect of pile-up and electronic noise, for a cone size of $\Delta R = 0.4$, is 4.7 GeV. The performance of two algorithms for jet energy determination have been compared. The 'H1 method' applying weights to individual calorimeter cells provides a better energy resolution than the 'Benchmark method' which applies weights to the calorimeter compartments. The jet energy can be determined without prior knowledge of the particle level energy by using simple smooth functions describing the energy dependence of the calibration coefficients without deterioration of the energy resolution. The residual energy non-linearities in the calibration are smaller than 2% and 3% using the 'H1 method' and the 'Benchmark method', respectively. Effects of the order of few percent, that affect the extrapolation of the calorimeter calibration for very high-p_T jets, beyond the reach of *in situ* calibration, have been discussed.

9.1.2 Jet algorithms

In this section, various types of jet algorithms are introduced and some of their basic properties are discussed in the context of the reconstruction of a sample of medium-p_T W's, for which the two decaying jets are in general well separated. More specific aspects linked to jet overlap or effects of final state radiation are discussed in Section 9.3 (mass reconstruction) and Section 12.5.1 (jet energy scale).

9.1.2.1 Description of a representative set of jet algorithms

There are two basically different approaches used in jet algorithms. The classical 'cone' algorithm which builds a jet around a seed which is representative of the core of the jet and identified usually as the tower with highest E_T. The 'K_T clustering' algorithm [9-14] starts from the full set of final hadrons, approximated by the towers in the calorimeter, and pairs the 'closest' ones, the distance being evaluated typically as $d_{ij} = min(E_{Ti}^2, E_{Tj}^2)((\Delta\eta_{ij})^2 + (\Delta\phi_{ij})^2)$, and progressively merges all 'particles' into jets.

The cone algorithm has several variants. The most basic approach consists of using the tower with the highest E_T as the jet seed and building a cone around that seed. Cells belonging to the cone are not available for subsequent jet finding. The parameters are the E_T^{seed} cut, the cone opening radius and the minimum E_T of the jet. Usually the centroid of the jet is recalculated from the list of towers contained in the cone. This is the baseline algorithm used by ATLFAST. An improvement to this simple approach is obtained by iterating the position of the centroid of the cluster and the corresponding cone. Various strategies for jet energy sharing or jet merging in the case of close jets or hard final state radiation have been considered.

Variants of the K_T clustering algorithm use different merging criteria [9-10], and different ways of ending the merging process, for example applying a cut on the distance or stopping at a certain predefined jet multiplicity. Intrinsically, there is no predefined jet size in this clustering algorithm and the actual size of the jet will vary from event to event adapting to the fragmentation or the presence of final state radiation. This clustering algorithm follows a combinatorial approach that requires looping many times over the towers and therefore is more time consuming than the cone algorithm.

In a third strategy, all towers are classified in order of decreasing E_T. The first tower is assigned to the first cluster, the next tower will be assigned to the same cluster or a new one depending on the distance $\Delta R = \sqrt{(\Delta\eta)^2 + (\Delta\varphi)^2}$. One parameter of the algorithm is the 'resolution', the minimum distance between two jets. All towers in the list are sequentially assigned to the closest cluster or a new cluster is started, the cluster centroid being re-evaluated each time a tower is added. This mechanism provides automatically energy sharing, while the shape and size of the cluster are not predefined. Optionally a fixed cone size can be required. This algorithm is described in [9-15] and will be referred to as MGS in the figures.

9.1.2.2 Performance of the jet algorithms

The performance of various algorithms is reviewed in this section. The following cases have been considered: the fixed cone algorithm (ΔR = 0.4 and 0.7), the K_T clustering algorithm with a distance parameter R_{cut} used to stop cell merging set to 0.4, and the MGS algorithm with the two-jet resolution parameter ΔR set to 0.3 (see [9-10] for a more detailed description of the parameters).

The differences arising from the jet algorithms are illustrated here using a sample of W+jet events with p_T^W larger than 100 GeV. A minimum E_T of 20 GeV was required for the partons. The range of E_T^{parton} studied in this sample extends from 20 to about 200 GeV. Figure 9-17 shows the angular distance ΔR between the two jets.

Results from a particle level study using ATLFAST at low luminosity are shown in Figure 9-18. The cone algorithm with $\Delta R = 0.7$ shows the best performance in that energy range: the ratio of reconstructed jet energy to parton energy is almost independent of energy and close to 1. The cone algorithm with $\Delta R = 0.4$ shows losses varying from 10% at low E_T to about 3% at 200 GeV. The K_T and the MGS algorithms show a flatter distribution in E_T but with an average loss of about 8%.

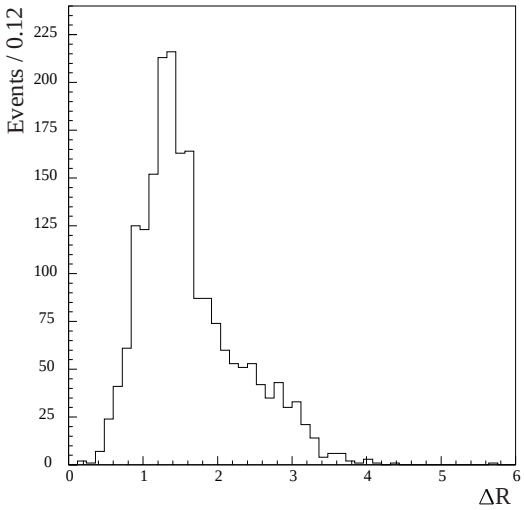

Figure 9-17 Distance in η–φ space between the two partons from W decays in W+jet events. The average angular opening between the jets is 1.6.

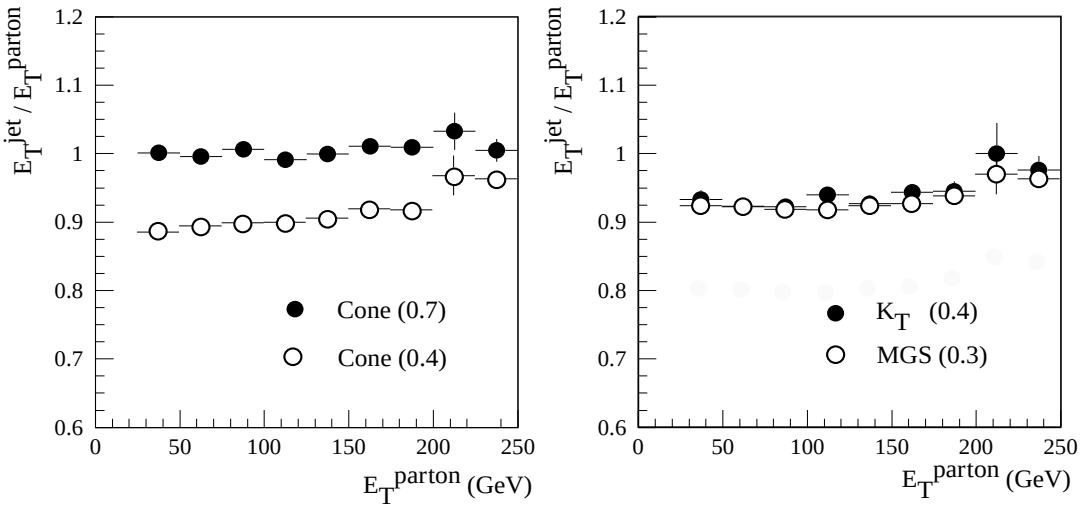

Figure 9-18 Reconstructed E_T of the jet divided by the E_T of the parton for the W+jet sample: the left figure compares the results of the fixed cone algorithm with cone size $\Delta R = 0.7$ and $\Delta R = 0.4$; the right figure shows the results of the K_T algorithm ($R_{cut} = 0.4$) and the MGS algorithm (resolution $\Delta R = 0.3$).

The effect of minimum-bias events has been studied by adding an average of 50 minimum-bias events generated with PYTHIA (with Poisson fluctuations). This number of events corresponds roughly to the effective number of minimum bias events obtained when applying the calorimeter shaping functions. The events were simulated by ATLFAST and added at the level of the projected E_T ($\Delta\eta \times \Delta\phi$) matrix. A p_T cut of 2 GeV per tower was applied. The result is shown in Figure 9-19. The cone algorithm with $\Delta R = 0.7$ suffers most from the effect of pile-up. For a cone size $\Delta R = 0.4$, the shift in the reconstructed jet transverse energy, compared to the case without pile-up, is about 12% at 40 GeV and 2% at 100 GeV. The effect is slightly smaller in the case of the K_T algorithm. The same is true for the MGS algorithm even though it has a variable jet size.

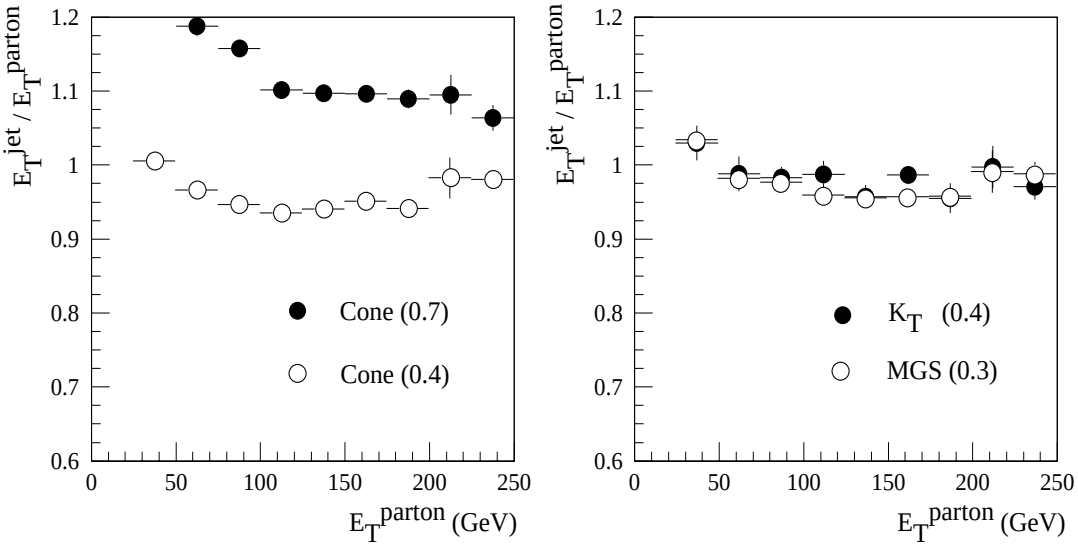

Figure 9-19 Reconstructed E_T of the jet divided by the E_T of the parton for the W+jet sample, with an average of 50 pile-up events added to the events and with an E_T tower cut of 2 GeV: the left figure shows the results of the fixed cone algorithm with cone size $\Delta R = 0.7$ and $\Delta R = 0.4$; the right figure shows the results of the K_T algorithm ($R_{cut} = 0.4$) and the MGS algorithm (resolution $\Delta R = 0.3$).

The figures demonstrate that the conversion from jet energy to parton energy depends on the jet algorithm and on the amount of pile-up. Differences of the order of 10% may arise, the low-E_T end of the spectrum being most affected. In addition, the underlying physics affecting the relation of the jet energy to parton energy, such as the parton shower process and the subsequent hadronisation together with initial state and final state radiation, depends on the physics process and introduces additional differences. The issue of the calibration of the jet energy scale with different physics processes is discussed in Section 12.5.

9.1.3 Low-p_T jet reconstruction

The ability to veto events by detecting the presence of additional low-p_T jets is a powerful tool for the reduction of the background in many physics channels. An example of the power of a jet veto is the case of Z+jet(s) events where the p_T balance between the Z and the jet can be used for *in situ* jet energy calibration, but multi-jet final states have to be vetoed efficiently to avoid biases in the correction. Another example is the rejection of $t\bar{t}$ background that, due to its large cross-section, affects many rarer physics processes. $t\bar{t}$ events tend to have high jet multiplicity and jets with small transverse energy. An efficient detection of these jets down to low-p_T is needed for a good rejection of that background.

A study of the jet veto efficiency in Z+jets was carried out with ATLFAST and full simulation (see Section 12.5.1.3 for more details). The standard fixed cone algorithm with cone size $\Delta R = 0.7$ was used. Figure 9-20 shows the fraction of events where more than one jet is reconstructed as a function of the p_T threshold applied. In the full simulation, jets are reconstructed starting from the projected E_T matrix in ($\Delta\eta \times \Delta\phi$) with the calorimeters being calibrated at the EM scale. Figure 9-2 shows that the reconstructed jet energy is typically of the order of 80% of the particle

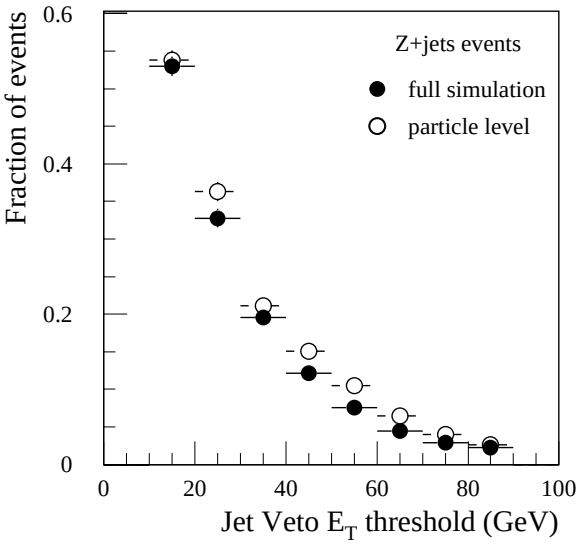

Figure 9-20 Fraction of events from the *Z*+jet(s) sample where more than one jet is reconstructed as a function of the p_T threshold applied. The black circles are for fully simulated events and the open circles are for particle level simulation with ATLFAST.

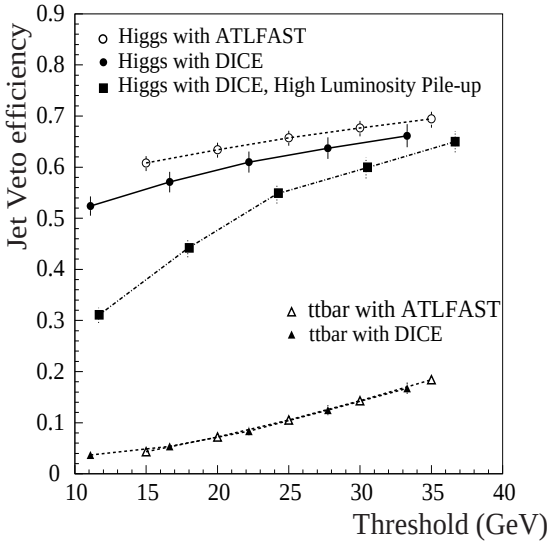

Figure 9-21 Comparison of the jet veto efficiency for the Higgs signal and the $t\bar{t}$ background obtained at particle level (open dots and triangles, respectively) and with full simulation (black dots and triangles) for low luminosity. For the Higgs signal, the black squares show the efficiency at high luminosity.

level jet energy. A good agreement is found between ATLFAST and the full simulation when this factor is taken into account to define the equivalent p_T threshold in the two sets of data, as seen in Figure 9-20.

Particle level and full simulation studies have been carried out in the search for a heavy Higgs signal ([9-16], [9-17], Section 19.2.10.2). The relatively low jet activity in the central region in this case can be used to reject the backgrounds, specifically $t\bar{t}$ events which have two additional jets. The efficiency of a jet veto, applied in the central region ($|\eta| < 2$), has been studied as a function of the jet p_T threshold. The jet veto efficiency, defined as the fraction of events with no additional jet with p_T larger than the threshold, is given in Figure 9-21. At low luminosity, the particle level simulation gives efficiencies that are about 5% higher than the efficiency obtained for the fully simulated Higgs signal. For the background of $t\bar{t}$ events, the agreement between particle level and full simulation is good. At low luminosity the jet veto threshold can be lowered to 15 GeV without losing much efficiency for the signal and while retaining a good rejection of the background. In the presence of high luminosity pile-up, minimum-bias events tend to generate low-p_T jets and the jet veto threshold has to be raised to 25 GeV to avoid a significant loss of efficiency for the signal (see Figure 9-21).

9.1.4 Forward jet tagging

Jet tagging at large pseudorapidities is one of the main tools to reduce backgrounds in the search for a heavy Higgs. For large Higgs masses [9-16][9-17], the dominant production process is vector boson fusion: $q\bar{q} \rightarrow q'\bar{q}'W_L W_L \rightarrow q'\bar{q}'H$. The two accompanying jets are typically detected in the region $2 < |\eta| < 5$. This region is covered by the end-cap and FCAL calorimeters.

The granularity of the End-cap Calorimeter is (0.1×0.1) in ($\Delta\eta\times\Delta\phi$) for $|\eta| < 2.5$, and (0.2×0.2) for larger rapidities. The cells are projective in pseudorapidity and azimuthal angle. This allows the use of fixed transverse energy cuts in the jet finding. On the other hand, the FCAL read-out cells do not have a projective geometry in pseudorapidity and azimuthal angle, but are constructed as cells in *x* and *y*, as shown in Figure 9-22. There are two tile sizes in two regions: one from $|\eta| \approx 3.2$ to $|\eta| \approx 4.2$ and the other from $|\eta| \approx 4.2$ to the acceptance limit at $|\eta| \approx 4.9$. Therefore it is not possible to apply a fixed E_T cut on the calorimeter towers since the tile sizes change continuously in pseudorapidity space. It is important to note that even if the towers were projective, the use of fixed E_T cuts would not be optimal. This is due to the fact that in the very forward regions, the lateral spread of the hadronic showers becomes very significant. This can be seen in Figure 9-23 which shows the reconstructed jet p_T inside a cone compared to the total p_T reconstructed in the FCAL. Energy losses at large pseudorapidities are clearly seen. The effect depends on the cone radius; the smaller the cone, the larger the losses due to the lateral shower size. On the other hand, the intrinsic response of the calorimeter is rather linear, as can be seen in Figure 9-24 which shows the total jet signal in the calorimeter calibrated at $|\eta| = 4.1$ with $E = 1000$ GeV jets using one calibration factor for each of the three FCAL compartments. Deviations from non-linearity appear only in the low-energy range: about 10% at 200 GeV and 20% at 100 GeV. Howev-

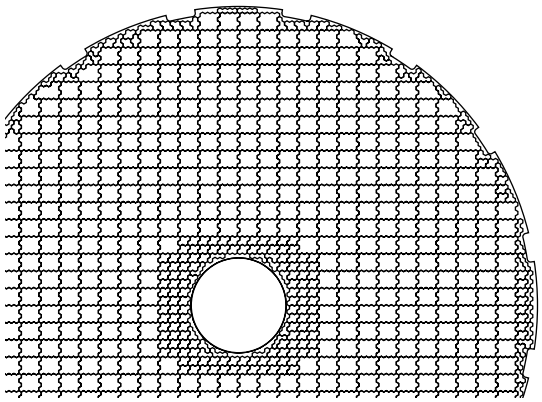

Figure 9-22 Tile read-out scheme in *x* and *y* for the FCAL.

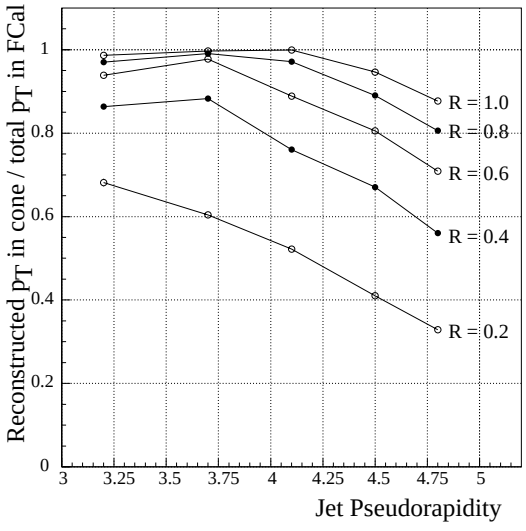

Figure 9-23 Reconstructed jet p_T inside a cone normalised to the total p_T reconstructed in the FCAL as a function of pseudorapidity and for various cone sizes. The sample of jets used here are back-to-back di-jet events (see Section 9).

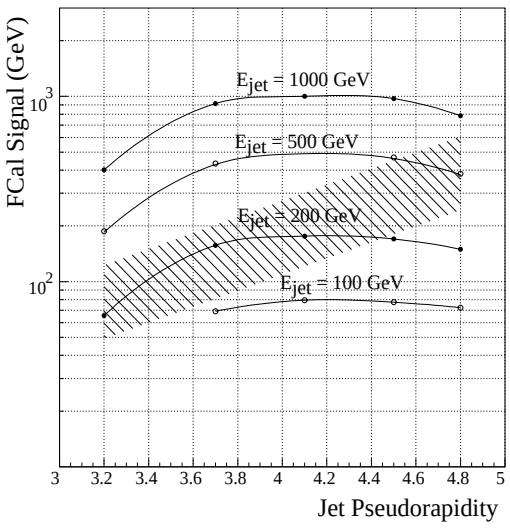

Figure 9-24 Total energy measured in the FCAL for various jet energies at different values of pseudorapidity. The calibration coefficients have been adjusted for $E = 1000$ GeV jets at $|\eta| = 4.1$. The hatched area represents the rms contribution of high luminosity pile-up events in cones of $\Delta R = 0.4$ to $\Delta R = 1.0$.

er, these low energies are not relevant for the FCAL as can be seen from the hatched area in the figure that represents the rms of high luminosity pile-up in jet cones of $\Delta R = 0.4$ to $\Delta R = 1.0$. Cuts based on the significance of the signal in the cells are more appropriate for the FCAL, the significance being defined as the signal divided by the rms of the (high luminosity) pile-up noise collected in a given cell.

The forward tagging efficiency has been studied with fully simulated events in the case of a 1 TeV Higgs produced via vector boson fusion where the two associated quarks are detected typically in the region $2 < |\eta| < 5$ (see [9-17] and Section 19.2.10.2). At lower rapidities $2 < |\eta| < 2.9$, in the End-cap Calorimeter, jets are tagged in the standard way. Each 0.1×0.1 tower in $(\Delta\eta \times \Delta\phi)$ above a 3 GeV E_T threshold was considered as a potential jet seed. This threshold was 6 GeV when pile-up noise was included. The energy of each tower within a radius of $\Delta R = 0.4$ was added to the energy of the jet candidate. An E_T threshold of 1.5 GeV was imposed on the energy in the towers when pile-up was included. The energy of the jet was calibrated without pile-up noise using the known value of the quark energy. The jet energy scale was adjusted to take into account the effect of the cuts and pile-up noise. Finally, a jet had to have a minimum corrected transverse energy of 15 GeV to be 'tagged'.

In the region $2.9 < |\eta| < 4.9$, in the FCAL, the energies deposited in each tube of a given tile were summed to form the cell signal. The pile-up energy rms was calculated for each tile in the three longitudinal segments separately. The jet reconstruction proceeded as follows: tiles having a significance higher than four were considered as potential jet seeds. The significance was defined as the signal divided by the rms of the high luminosity pile-up noise collected in the cell. This cut could go as high as 10 when high luminosity pile-up noise was added (see left plot of Figure 9-25). The energy in a tile was added to the candidate jet energy if its significance was greater than 1.0 and it was within a radius of $\Delta R = 0.4$ of the seed cell. With pile-up noise, a cut was imposed on the significance in a $\Delta R = 0.2$ cone around the seed cell (see right plot of

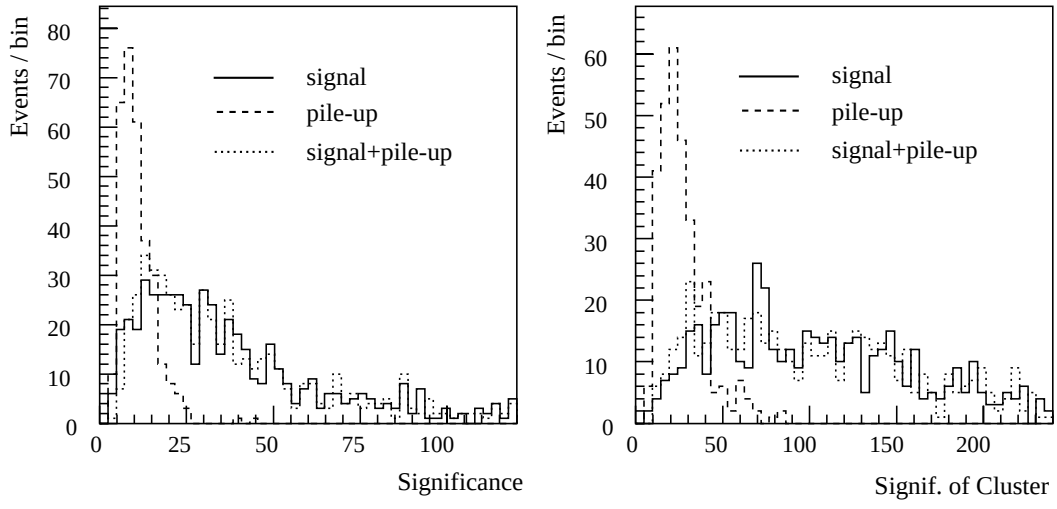

Figure 9-25 The left plot shows the significance of the jet seed cell in the FCAL region. The significance is defined as the signal divided by the rms of the high luminosity pile-up noise collected in the cell. The right plot gives the total significance in a $\Delta R = 0.2$ cone (the sum is linear) around the seed cell.

Figure 9-25). This cut proved to be the most efficient discriminator between pile-up jets and signal jets. Finally, after calibration and the adjustment of the energy scale, which depended on the cuts used, a corrected transverse energy of 15 GeV was required for the jet to be tagged.

The results obtained with this procedure for the case of the 1 TeV Higgs are described below. In the upper plot of Figure 9-26, it is important to note that the average p_T of forward quarks decreases as a function of pseudorapidity and that the tagging efficiency is not only a function of the calorimeter acceptance alone but depends also on the kinematics of the physical process considered. Therefore, the jet tagging efficiencies obtained here are not directly applicable to other physics processes. The lower plot of Figure 9-26 gives a comparison of the jet tagging efficiency without pile-up between the full simulation and ATLFAST. The ATLFAST results show good agreement with the full simulation up to $|\eta| = 4.0$. Beyond this value, the transverse shower development leads to energy losses in the full simulation. The lower plot of Figure 9-26 shows also the forward jet tagging efficiency obtained when high luminosity pile-up is included. The various significance cuts described earlier, as well as an energy cut on the tagged jets in addition to the E_T cut, were tuned to optimise the jet efficiency while keeping the fake jet rate at the level of 10% in the whole $2 < |\eta| < 5$ range. Compared to the low luminosity case the efficiency decreases by less than 10%.

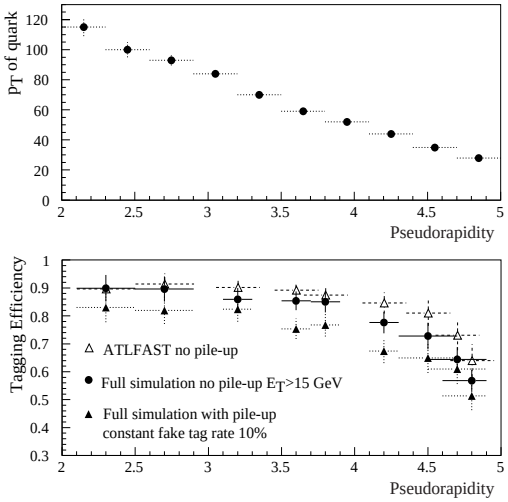

Figure 9-26 The upper plot shows the average p_T of forward quarks produced in association with a 1 TeV Higgs. The lower plot gives the jet tagging efficiency for particle level and full simulation at low luminosity for a 15 GeV E_T threshold. It also shows the jet tagging efficiency obtained with high luminosity pile-up, adjusting selection cuts to maintain a constant fake rate of 10% across pseudorapidity.

9.1.5 τ identification and measurement

Efficient reconstruction and identification of all lepton species are crucial at the LHC. τ-leptons are the most difficult ones in this respect, since they produce neutrinos and hadrons among their decay products. An example of the relevance of τ identification is given by the fact that, over a large region of the MSSM parameter space, the heaviest Higgs bosons can only be observed through their decays to pairs of τ-leptons ($H/A \rightarrow \tau\tau$, $H^{\pm} \rightarrow \tau\nu$). The sensitivity to these channels depends strongly on the quality of the τ identification, since backgrounds from jets are potentially very large (see Chapter 19).

The τ identification capability of ATLAS was evaluated by using fully-simulated events containing a Higgs boson A decaying to ττ, where one of the τ's decays hadronically and the other leptonically.

The τ identification is based on criteria, such as shower shape in the calorimeters, that can be evaluated realistically only by using a detailed GEANT-based simulation of the detector response. Therefore, high-statistics samples of fully-simulated events were used for this study.

They consisted of ~21 000 $H/A \rightarrow \tau\tau$ signal events (direct A production and $b\bar{b}A$ associated production), corresponding to eight different A masses in the range 100-500 GeV, and of ~11 000 background events ($t\bar{t}$, $b\bar{b}$, W+jets). About 16 000 τ's and 15 000 jets with $E_T > 30$ GeV and $|\eta| < 2.5$ were available in the signal and background samples respectively [9-18][9-19]. In addition, a sample of ~26 000 jets from QCD processes was used. Finally, a sample of 1000 isolated τ's decaying to hadrons, generated at fixed $p_T = 60$ GeV and $\eta = 0.3$ ('single τ's'), was used for some checks. Low-luminosity operation was assumed in most cases, therefore approximately two minimum-bias events were superimposed on the fully simulated events.

9.1.5.1 τ reconstruction

A jet was labelled as a τ-jet if the distance ΔR of the jet barycentre from the barycentre of the hadronic part of the τ decay ($h\tau$), as computed at particle level, was less than 0.3. By applying this criterion, 98% of τ's from $A \rightarrow \tau\tau$ events with $p_T(h\tau) > 30$ GeV were labelled as τ-jets. The τ-jet energy was reconstructed from the calorimeter cell energies, by applying the same calibration constants as used for the QCD jet reconstruction (Section 9.1). As a consequence, the τ energy was overestimated by ~5% because the electromagnetic content of a τ-jet is on average larger than that of a normal jet. The τ transverse momentum was defined as the p_T of the visible decay products. The τ charge was calculated from the charge of the associated tracks. Using the reconstructed tracks associated to the jet within a cone of size $\Delta R < 0.4$, the weighted jet charge was defined as the sign of $\Sigma_i |p_i| q_i$, where q_i is the charge of a track of momentum p_i. In this way, the sign of the τ charge was determined correctly in 92% of cases.

9.1.5.2 τ identification

Jets from hadronic τ decays and QCD can be distinguished by using the information from the Calorimeters and the Inner Detector. Since hadronic τ decays are characterised by low multiplicity (in 77% of the cases only one charged track is produced), a τ-jet consists in general of a well-collimated calorimeter cluster with a small number of associated charged tracks. The following variables were used to distinguish τ-jets from normal jets:

- R_{em}, the jet radius computed using only the electromagnetic cells contained in the jet. It is defined as

$$R_{em} = \frac{\sum_{i=1}^{n} E_{T_i} \sqrt{(\eta_i - \eta_{cluster})^2 + (\phi_i - \phi_{cluster})^2}}{\sum_{i=1}^{n} E_{T_i}}$$

where i runs over the cells of the EM Calorimeter contained in a cone of size $\Delta R = 0.7$ around the barycentre of the cluster, the coordinates of which are $(\eta_{cluster}, \phi_{cluster})$.

- ΔE_T[12], the fraction of transverse energy in the EM and hadronic calorimeters, which is contained in a region defined by $0.1 < \Delta R < 0.2$ around the barycentre of the cluster. This is an isolation criterion.

- N_{tr}, the number of charged tracks with p_T above a given threshold (1, 2 and 5 GeV were used), pointing to the calorimeter cluster within $\Delta R = 0.3$.

The performance for τ/jet separation was studied in two cases, which are discussed below. The first case is for $A \rightarrow \tau\tau$ searches, where very stringent τ identification criteria must be adopted, since a large rejection of the potentially large background is crucial. Here the goal was to select a very pure τ sample, with a small contamination of QCD jets. In the second case, the τ efficiency was studied as a function of the jet rejection over a broad range of efficiencies and rejections. This gives rise to τ samples of different purities which can be used in a variety of physics channels according to the specific requirements.

τ / jet separation for $A \rightarrow \tau\tau$ searches

A jet with $E_T > 30$ GeV and $|\eta| < 2.5$ was identified as a τ-jet if it satisfied the cuts on R_{em}, ΔE_T^{12} and N_{tr} listed in Table 9-7. This table also shows the cumulative efficiency of these cuts for τ-jets from direct and associated A production, for QCD jets and for the jets contained in typical background events to the $A \rightarrow \tau\tau$ channel.

Table 9-7 τ identification criteria used in the search for $A \rightarrow \tau\tau$ events and their cumulative efficiency (in percent) for various signal and background samples at low luminosity.

Variable	Cut	$b\bar{b}A \rightarrow \tau\tau$	$A \rightarrow \tau\tau$	QCD jets	*b*-jets	$t\bar{t}$	*W*+jets
$<p_T>$ of τ–jet (GeV)		80	73	44	58	65	52
R_{em}	< 0.07	56 ± 1	45 ± 1	1.1 ± 0.1	1.9 ± 0.4	1.3 ± 0.2	2.9 ± 0.5
ΔE_T^{12}	< 0.1	40 ± 1	32 ± 1	0.6 ± 0.05	0.9 ± 0.2	0.7 ± 0.2	1.8 ± 0.5
N_{tr} ($p_T > 2$)	= 1	21 ± 1	17 ± 1	0.09 ± 0.02	< 0.06	0.08 ± 0.06	0.6 ± 0.3
N_{tr} ($p_T > 2$)	= 1 or = 3	32 ± 1	25 ± 1	0.19 ± 0.03	0.18 ± 0.1	0.2 ± 0.1	1.1 ± 0.3

The criteria based on the calorimeter information (R_{em} and ΔE_T^{12}) provide a rejection of about 170 against QCD jets for an efficiency of 40% for hadronic τ decays. This performance can be further improved by cutting on the number of tracks associated with the calorimeter cluster. In the Inner Detector, tracks belonging to a low-multiplicity jet are expected to be reconstructed with high efficiency and negligible fake-track rate down to $p_T = 1$ GeV even at the highest luminosities expected at the LHC [9-20]. Therefore, by requiring only one track with $p_T > 2$ GeV associated to the calorimeter cluster, it was possible to improve the rejection against jets by a factor between three and nine, depending on the physics channel. This performance can be further improved by identifying photon conversions, which was not done for the study presented here. On the other hand, requiring one or three tracks associated to the calorimeter cluster increases the τ efficiency by a factor of 1.5, but does not improve the overall sensitivity because the jet background increases by a factor larger than two. These results were obtained by using generated tracks. When tracks reconstructed in the Inner Detector are used, the number of τ's with one associated track increases by 10%, due to inefficiencies in the track reconstruction. For one-prong τ decays, the reconstructed track with the largest p_T is within ±5 GeV of the generated track with the largest p_T in 87% of cases. The impact of varying the track p_T cut was also studied: results are not significantly different for 1, 2 or 5 GeV thresholds [9-19].

The rejection against jets in $t\bar{t}$ events is larger than the rejection against jets in *W*+jet events, due to the different jet type (quark or gluon) and p_T distribution. The *b*-jet rejection is larger than the rejection against light-quark or gluon jets.

The results shown in Table 9-7 were obtained by using all clusters with $p_T > 30$ GeV and $|\eta| < 2.5$ reconstructed in the signal and background events. For a fixed set of selection cuts, the τ identification efficiency increases with increasing p_T (from 15 to 130 GeV) and the jet rejection shows a fast increase with p_T up to 20 GeV and a smooth dependence above. The τ efficiency depends also on the pseudorapidity, being higher in the central region of the acceptance [9-19].

According to preliminary studies, additional selection cuts based on the information from the strip section of the EM Calorimeter [9-19] provide no significant improvement on the τ efficiency and jet rejection. This is due to the strong correlation with the criteria discussed above. However, the use of the η-strips for τ identification was not optimised for the study presented here, and it is not excluded that further work may lead to some improvement in the performance.

τ efficiency versus jet rejection

The jet rejection which can be achieved as a function of the τ identification efficiency was studied by applying several different selection criteria, based on the variables R_{em}, ΔE_T^{12} and N_{tr} ($p_T > 2$ GeV), in order to cover values for the τ efficiency in the range 10% to 90%. Samples of τ's from $b\bar{b}A$ events and jets from QCD processes were used.

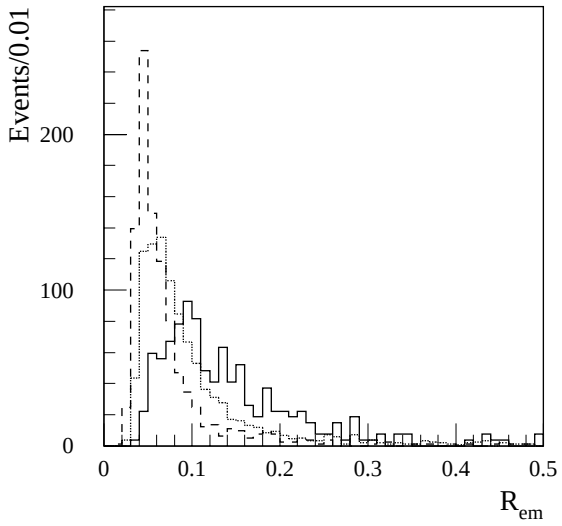

Figure 9-27 R_{em} distribution for τ-jets with different p_T: $15 < p_T < 30$ GeV (full line), $30 < p_T < 70$ GeV (dotted line) and $70 < p_T < 130$ GeV (dashed line). All distributions are normalised to the same number of events.

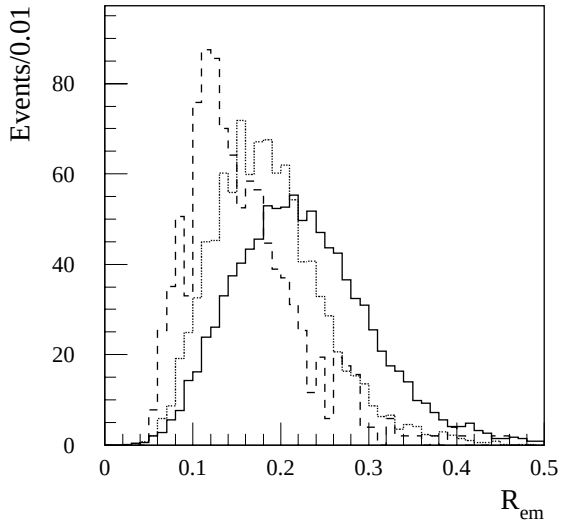

Figure 9-28 As Figure 9-27 but for QCD jets.

Due to the p_T dependence of the τ identification performance, results are given for different p_T ranges. As an example, Figures 9-27 and 9-28 illustrate how the R_{em} distribution changes with the transverse momentum of τ-jets and QCD jets respectively. In both cases, the distribution becomes narrower at high p_T, therefore the τ efficiency increases with p_T whereas the jet rejection decreases. This behaviour can be inferred also from Figures 9-29 and 9-30, in which the τ identification efficiency and the jet rejection are presented as a function of the cut on R_{em} only. The ΔE_T^{12} distribution has little p_T dependence. The N_{tr} distribution for τ's does not depend on p_T, whereas N_{tr} increases with p_T in the case of jets.

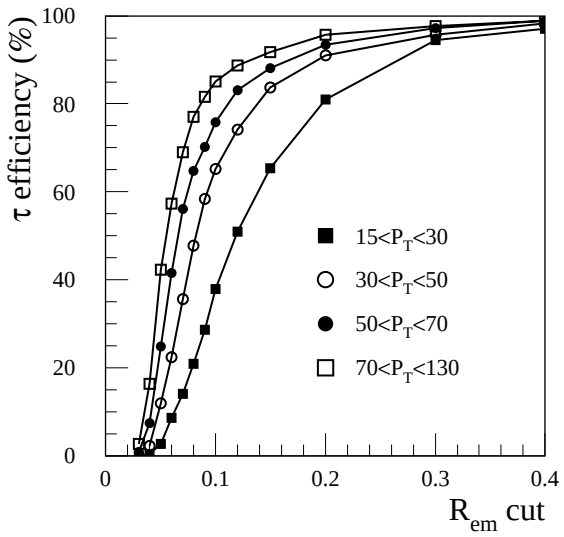

Figure 9-29 τ identification efficiency, as a function of the cut on R_{em}, for various p_T ranges.

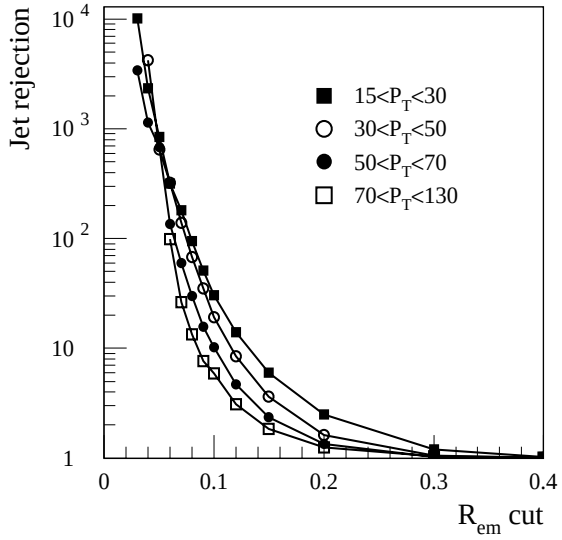

Figure 9-30 Jet rejection, as a function of the cut on R_{em}, for various p_T ranges.

The total jet rejection, obtained in different p_T ranges, is shown in Figure 9-31 as a function of the τ identification efficiency. Straight-line fits are superimposed to each set of points and can be used to parametrise the detector performance [9-21]. As expected, as p_T increases the curves shift towards larger τ efficiencies, for the same jet rejection.

The dependence of the τ efficiency on pseudorapidity was also considered. Whilst the jet rejection does not show any pseudorapidity dependence, the average τ identification efficiency over the full pseudorapidity coverage ($|\eta| < 2.5$) is very similar to the efficiency over the region $0.7 < |\eta| < 1.5$, whereas the efficiency is larger for $|\eta| < 0.7$ and smaller for $|\eta| > 1.5$.

Finally, the efficiency for single τ's is larger than that for τ's from complete physics events. For instance, the R_{em} distribution peaks at larger values for τ's from complete physics events than for single τ's. This is also due to the choice of a relatively large cone ($\Delta R = 0.7$) for the τ-jet reconstruction, so that other particles from the rest of the event contribute to the τ-jet. As a consequence, with the selection criteria used for the $A \rightarrow \tau\tau$ study reported above, the τ identification efficiency for single τ's is a factor ~1.5 larger than for τ's in physics events.

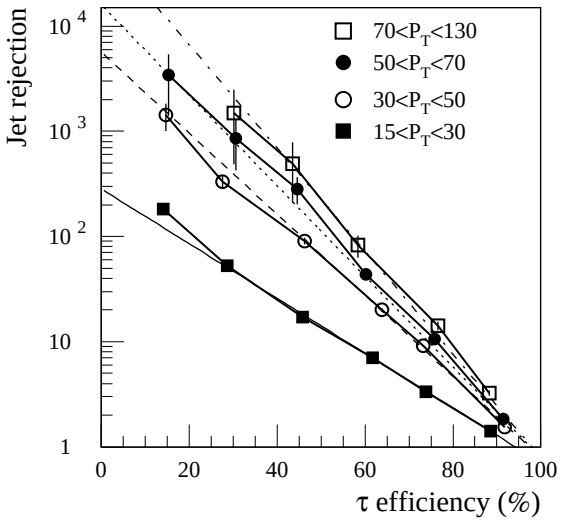

Figure 9-31 Jet rejection as a function of the τ efficiency, as obtained over the region $|\eta| < 2.5$ and in various p_T ranges. Straight-line fits are superimposed.

9.1.5.3 τ veto

The capability of vetoing events containing τ's should be useful for many physics studies at the LHC, for instance to reject backgrounds (*e.g.* $W \rightarrow \tau\nu$) to some SUSY channels (Chapter 20).

A study of the τ veto performance was made as a function of p_T, since the difference in the τ identification variables, in particular R_{em}, for τ's and jets decreases with decreasing p_T. The results are shown in Figures 9-32 and 9-33.

By requiring $N_{tr} > 3$ and $R_{em} > 0.08$, a jet efficiency of about 90% was achieved for $p_T > 60$ GeV and for a τ efficiency of only 5%. At lower p_T, a τ efficiency of 5% was obtained with a lower jet efficiency. A jet efficiency of 90% can be reached in this case only with a significant increase of the τ efficiency.

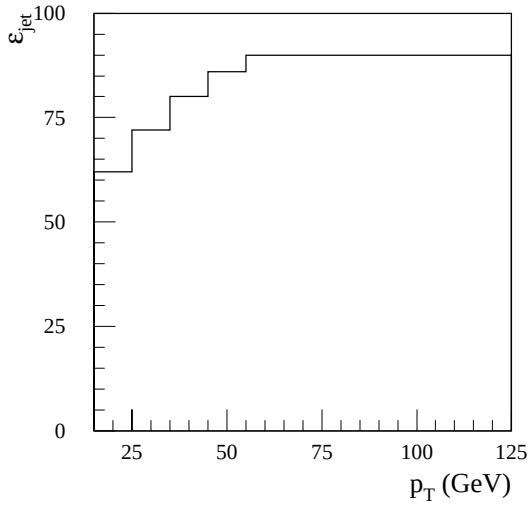

Figure 9-32 Jet identification efficiency, as a function of p_T, for a fixed τ efficiency of 5%.

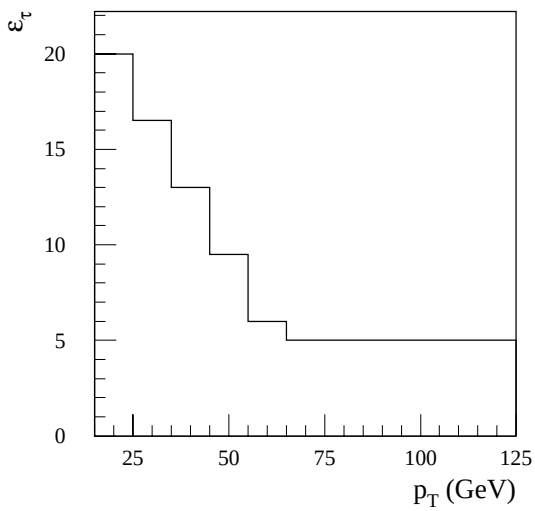

Figure 9-33 τ identification efficiency, as a function of p_T, for a fixed jet efficiency of 90%.

9.1.5.4 Performance at high luminosity

The jet rejection and τ efficiency performance at high luminosity were studied by using $A \rightarrow \tau\tau$ events. For this purpose, fully-simulated pile-up events (Chapter 2) were superimposed on the physics events. A threshold of ~2.5σ of the pile-up noise was applied to the energy deposited in the calorimeter towers. Towers were formed in each calorimeter by using the granularity of the longitudinal compartment with the coarsest granularity and by adding longitudinally all cells belonging to that calorimeter.

For the low-luminosity study, the R_{em} and ΔE_T[12] variables were defined using the cell information in the various compartments, while for the high-luminosity case they were based on the tower information. This latter procedure gives a non-optimal definition of both variables but simplifies the use of energy thresholds. It was also assumed that the number of tracks with $p_T > 2$ GeV is not affected when pile-up is added. After re-optimisation of the τ identification cuts, τ efficiency and jet rejection performances similar to the low-luminosity case were obtained at high luminosity [9-19].

9.1.5.5 Conclusions

Hadronic τ decays can be efficiently reconstructed and identified by using the information from the calorimeters and the Inner Detector. In general, the τ efficiency depends on p_T, pseudorapidity and the physics process. For a τ identification efficiency of ~20%, a rejection factor of 170 to 1 200 can be achieved against jets from W+jets and $t\bar{t}$ production and of about 1 700 against b-jets. This performance, which is similar at low and high luminosity, provides good sensitivity for the $A \rightarrow \tau\tau$ channel in the mass range 100 to 500 GeV (see Chapter 19). It is also possible to veto 95% of the τ's while mainting an efficiency of about 90% for all other jets.

9.2 E_T^{miss} measurement

Good measurement of the missing transverse energy is needed at the LHC for two reasons. Firstly, E_T^{miss} is an important signal for new physics, *e.g.* production and decay of SUSY particles, production and decay of the Higgs boson in the channel $H \rightarrow ZZ \rightarrow ll\nu\nu$. Therefore, minimisation of fake high-E_T^{miss} tails produced by instrumental effects, such as jets badly measured in a calorimeter crack, is mandatory in order to observe events characterised by genuine missing transverse energy. Secondly, in order to reconstruct a narrow invariant mass distribution for new (heavy) particles involving neutrinos among their decay products, good E_T^{miss} resolution is needed. One example is the possible production of an A boson followed by the decay $A \rightarrow \tau\tau$. The most critical experimental issues for a reliable and precise measurement of the event missing transverse energy are related to the performance of the calorimeters: good energy resolution, good response linearity and hermetic coverage are required.

9.2.1 E_T^{miss} resolution

The detector performance in terms of E_T^{miss} resolution was studied by using fully-simulated $H/A \rightarrow \tau\tau$ events in the H/A mass range 100–500 GeV. Typical E_T^{miss} values for these events are in the range 20-100 GeV [9-22].

Events were fully simulated in the pseudorapidity range $|\eta| < 3$. In the forward region $3 < |\eta| < 5$ the contribution of the calorimeter resolution to the accuracy of the E_T^{miss} measurement is small (Section 9.2.1.3) and the CPU needed for full simulation very large. Therefore, the detector response in this region was not fully simulated, but the particle energies were smeared according to the expected resolution. A check with 500 events with m_A = 150 GeV, fully simulated up to $|\eta| = 5$, was performed and gave similar results to the case where full simulation is done over $|\eta| < 3$ only. Fully-simulated (over $|\eta| < 5$) samples of minimum-bias events were used also for this study.

9.2.1.1 E_T^{miss} reconstruction

The x and y components of the E_T^{miss} vector (p_x^{miss}, p_y^{miss}) were obtained from the transverse energies deposited in the cells with $|\eta| < 3$, taking into account the additional contribution from the FCAL simulated at particle level as described above.

In the following sections, the most relevant issues for a good E_T^{miss} resolution are discussed one by one. Crucial elements are sufficient pseudorapidity coverage and an accurate calibration of all calorimeters, in particular in the region $|\eta| < 3$ which provides the dominant contribution to the E_T^{miss} resolution. The contribution of low-energy cells, such as cells outside jets, cannot be neglected, and the cell energy cut-off applied in the presence of electronic noise and pile-up has to be carefully tuned.

9.2.1.2 Calorimeter calibration

Particular attention was paid to the accurate calibration of all calorimeters and to the non-linearity of the response at low energy. The calibration accounts also for energy losses in the dead material in front of the calorimeters (*e.g.* cryostats) and at the transition between different calorimeter parts (cracks). The best E_T^{miss} resolution is achieved by using three sets of calibration constants for each calorimeter: one set for electromagnetic clusters, one set for hadronic clusters and one set for cells outside clusters. For the study presented here, however, cells outside clusters were calibrated in the same way as cells inside hadronic clusters. Therefore results are conservative, because the use of specific calibration constants for cells outside clusters, which provide a correction for the non-linearity of the calorimeter response to low-energy particles [9-18], improves the E_T^{miss} resolution by ~5%.

9.2.1.3 Calorimeter coverage

Calorimetric coverage up to $|\eta| = 5$ is essential for a reliable E_T^{miss} measurement [9-22]: the resolution of each component of the E_T^{miss} vector, as calculated at particle level for $A \rightarrow \tau\tau$ events with $m_A = 150$ GeV, degrades from 2.3 GeV to 8.3 GeV if the calorimeter coverage is reduced from $|\eta| < 5$ to $|\eta| < 3$.

On the other hand, the contribution of the forward region to the E_T^{miss} resolution is small, because the particle transverse energy decreases at large rapidity. The resolution of each component of the E_T^{miss} vector, as obtained with full simulation of $A \rightarrow \tau\tau$ events with $m_A = 150$ GeV [9-2], was found to be about 7 GeV (to be compared with 2.3 GeV at particle level), the main contribution coming from the barrel region (about 5 GeV), followed by the end-cap region (about 4 GeV) and the forward region (about 3 GeV).

The dead material in the transition region between the barrel and the end-cap calorimeters has no significant effect on the width of the core of the E_T^{miss} distribution. The impact of these regions on the high-E_T^{miss} tails is discussed in Section 9.2.2.

9.2.1.4 Electronic noise

When the electronic noise in the calorimeter is taken into account (Chapter 4), only cells with an energy larger than 1.5σ are considered for the E_T^{miss} reconstruction. The resulting resolution deteriorates by less than 10% compared to the resolution obtained without noise, the contribution of the noise amounting to about 3 GeV. A study of the optimum cell cut-off was performed. The E_T^{miss} resolution deteriorates by a factor ~1.3 if the cell cut-off is 2.5σ instead of 1.5σ. If cells outside jets, which are more than 50% of the occupied cells, are not included at all, the resolution of the two E_T^{miss} components degrades by a factor ~1.3.

9.2.1.5 Coherent noise

As discussed in [9-2], a coherent noise smaller than 3 MeV per channel (size: $\Delta\eta x\Delta\phi = 0.025x0.025$) in the EM Calorimeter gives no appreciable deterioration of the E_T^{miss} resolution and of the expected significance of a possible $A \rightarrow \tau\tau$ signal, provided that a reoptimisation of the cell energy cut-off is performed. For larger values of coherent noise, on the other hand, the E_T^{miss} resolution degrades in an unacceptable way. Therefore, a coherent noise of smaller than 3 MeV per channel is one of the requirements for the EM Calorimeter electronics (Chapter 4).

9.2.1.6 Results

The E_T^{miss} resolution was studied with $A \rightarrow \tau\tau$ events, which are characterised by a genuine E_T^{miss} due to the presence of neutrinos, at low luminosity, and with minimum-bias events, which do not contain physical sources of missing energy, at low and high luminosity.

The resolution $\sigma(p_{xy}^{miss})$ of each component of the E_T^{miss} vector is defined as $\sigma(\Delta)$ where

$$\Delta = \sum p_x(p_y)_{gen} - \sum p_x(p_y)_{rec} \qquad 9\text{-}7$$

where the first term on the right-hand side is the sum of the x (y) components of the momenta of all generated particles (neutrinos and muons excluded) without any pseudorapidity restriction, and the second term is the sum of the x (y) momenta as reconstructed from the calorimeters.

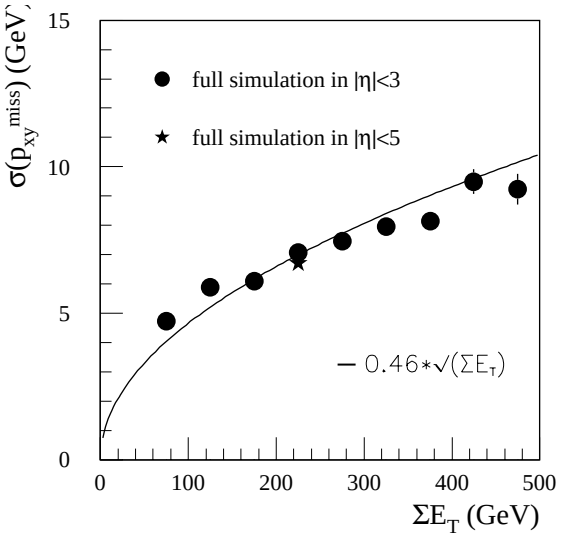

Figure 9-34 Resolution of the two components of the E_T^{miss} vector, as a function of the total transverse energy in the calorimeters, for $A \rightarrow \tau\tau$ events with m_A =150 GeV at low luminosity.

Figure 9-34 shows the dependence of $\sigma(p_{x,y}^{miss})$ on the total transverse energy measured in the calorimeters ΣE_T for $A \rightarrow \tau\tau$ events. The result obtained using full simulation over $|\eta| < 5$ is compared to the result obtained with full simulation over $|\eta| < 3$ only. No significant difference between the two approaches is observed. The electronic noise of the EM Calorimeter was included, and a low-energy cut-off at 1.5σ was applied to the transverse energy deposited in each cell. The resolution of the E_T^{miss} components varies between about 5 and 10 GeV when m_A varies between 100 and 500 GeV, which allows a good mass resolution from the reconstructed $A \rightarrow \tau\tau$ spectrum (Section 9.3.3.4), and therefore high sensitivity to this channel (see Chapter 19).

The points shown in Figure 9-34 can be fitted with the form

$$\sigma(p_{xy}^{miss}) = 0.46 \times \sqrt{\Sigma E_T}$$

where E_T is expressed in GeV. This result includes the effect of both the energy resolution and the limited coverage of the detector. If the contribution of the limited coverage is unfolded, then the resolution becomes $\sigma(p_{xy}^{miss}) = 0.39 \times \sqrt{\Sigma E_T}$.

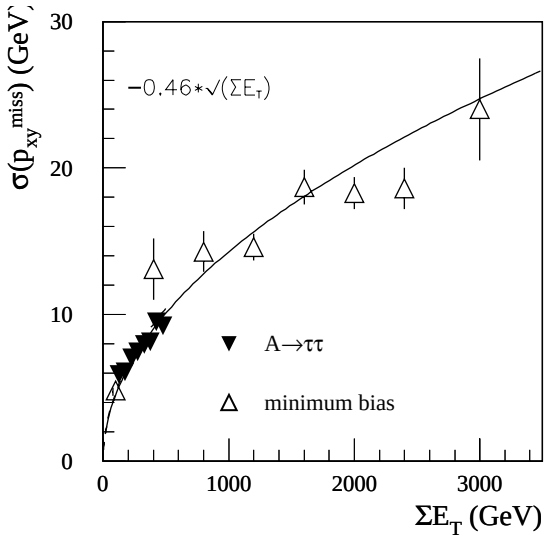

Figure 9-35 Resolution of the two components of the E_T^{miss} vector, as a function of the total transverse energy in the calorimeters, for minimum-bias events and $A \rightarrow \tau\tau$ events with m_A=150 GeV at low luminosity.

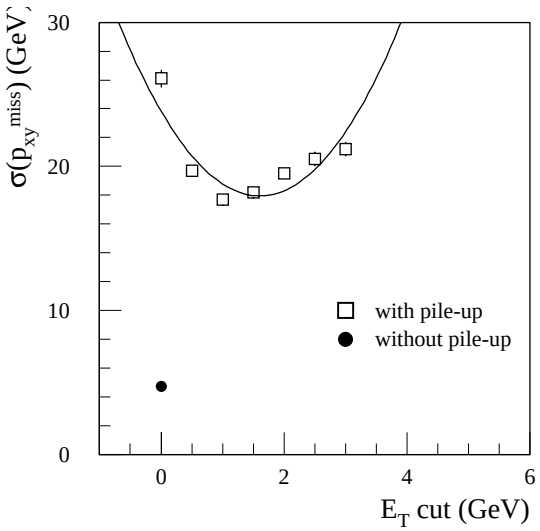

Figure 9-36 Resolution of the two components of the E_T^{miss} vector for $A \rightarrow \tau\tau$ events with m_A = 150 GeV at high luminosity, as a function of the tower E_T cut-off.

The dependence of the E_T^{miss} resolution on the total transverse energy measured with the calorimeters was also studied with minimum-bias events fully simulated in the region $|\eta| < 5$. Up to 48 minimum-bias events were combined to obtain a large total transverse energy in the calorimeters. The results obtained in this way are compared to the results from $A \rightarrow \tau\tau$ events in Figure 9-35: the agreement is good and the parametrisations obtained for both physics samples are the same. The conclusion of this study is that the E_T^{miss} resolution scales like $\sigma(p_{xy}^{miss}) = k \times \sqrt{\Sigma E_T}$ with $k \sim 0.46$.

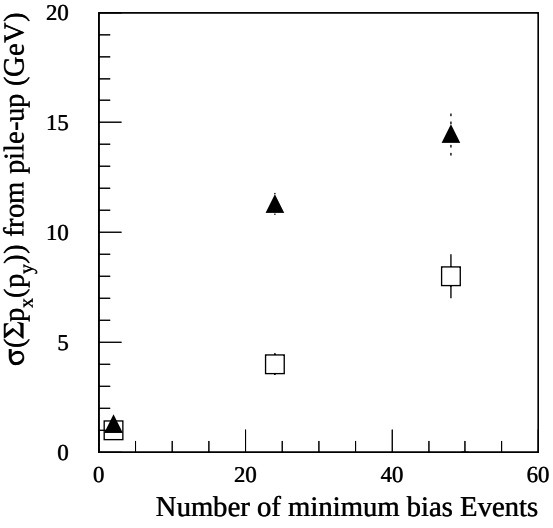

Figure 9-37 Contribution to $\sigma(p_{xy}^{miss})$ from the pile-up and electronic noise expected at high luminosity (closed symbols). The open symbols show the contribution of the FCAL alone. A cut-off E_T (tower) > 1 GeV was applied in both cases.

When the high-luminosity case was considered, the E_T^{miss} resolution was defined in the same way as in Equation 9-7, with the only difference that the reconstructed E_T^{miss} (second term of the right-hand side of Equation 9-7) was evaluated with the pile-up added in the calorimeters. The contribution of the pile-up in the forward region was neglected, because it is small after a tower energy cut-off is applied (see below). From this definition it is clear that the E_T^{miss} resolution is degraded by the presence of pile-up. The impact can be reduced by applying a cut-off on the energy content of the calorimeter towers. Figure 9-36 shows the dependence of $\sigma(p_{xy}^{miss})$ on the cut-off. The reso-

lution is best for a cut-off of ~1 GeV, which corresponds to about 2.5σ of the quadratic sum of the electronic noise and pile-up. Despite the cut-off, the performance is degraded by a factor of larger than two as compared to the low-luminosity case.

Figure 9-37 shows the contribution to $\sigma(p_{xy}^{\text{miss}})$ coming from the pile-up and electronic noise alone, as obtained by applying the optimum tower cut-off of 1 GeV. The contribution of the pile-up in the FCAL is small if a cut-off is applied, which justifies the choice of simulating the pile-up up to $|\eta| = 3$ only.

9.2.2 E_T^{miss} tails

The detection of large E_T^{miss} is an important signature in many physics channels. One example is the search for a heavy Standard Model Higgs boson with a mass in the range 500-700 GeV in the decay mode $H \rightarrow ZZ \rightarrow ll\nu\nu$. The decay of one of the Z bosons to two neutrinos generates large E_T^{miss} (see Section 19.2.10.1). In that context, one of the potentially dangerous backgrounds comes from Z+jet(s) events, where a badly measured jet could fake large E_T^{miss}. The rejection factor needed is of the order of 1000 in the region of E_T^{miss} larger than 200 GeV.

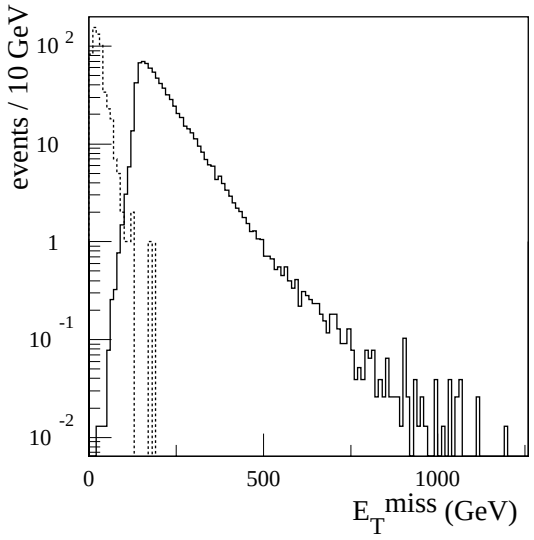

Figure 9-38 E_T^{miss} distribution from Z+jet events with $p_T^Z > 200$ GeV: the full line is for the case where the jet is undetected and the dashed for the fully simulated jets.

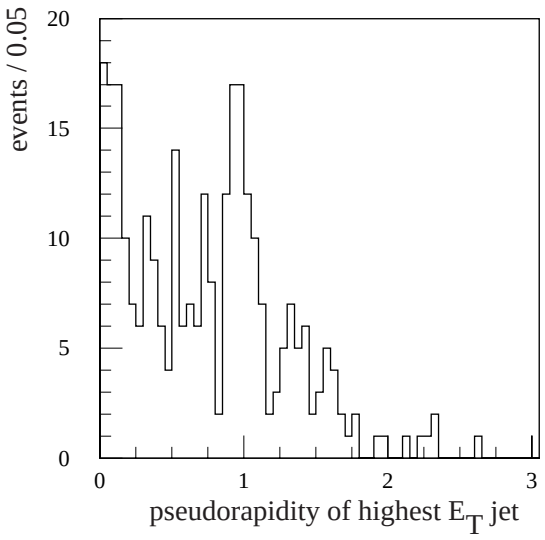

Figure 9-39 Pseudorapidity of the jet with the highest p_T for the events with E_T^{miss} larger than 50 GeV.

A sample of 4 667 Z+jet(s) events was fully simulated. A p_T cut of 200 GeV was applied to the Z at the generation level, and the Z was required to decay to two muons. Since the interest is in the impact that the calorimeter cracks and dead material could have on the measurement of E_T^{miss}, and therefore in using as many events as possible of the sample of fully simulated jets, no additional requirements on the p_T or pseudorapidity of the muons were set and the particle level muon momentum was used in the E_T^{miss} calculation. On the other hand, the probability of radiative muon processes is non-negligible for very energetic muons. In that case, the muons deposit energy in the calorimeter affecting the p_T balance. To eliminate radiative muons, events with a jet reconstructed within $\Delta R = 1$ of the direction of the muon were rejected. The particle-

level momentum of the muon was used, correcting simply for the average energy loss in the calorimeter. A sample of 3 826 events passed that selection. The resulting E_T^{miss} distribution is shown in Figure 9-38 as a dotted line. There are only two events with E_T^{miss} above 200 GeV. Those events contain a high-p_T neutrino, hence they contain genuine E_T^{miss}. The full line in the same figure represents the E_T^{miss} reconstructed in the event if the jet balancing the p_T of the Z would go completely undetected. It can be seen that the rejection factor of 1000 needed above 200 GeV is achieved. Figure 9-39 shows the pseudorapidity of the jet with the highest p_T for the events that have a E_T^{miss} larger than 50 GeV. Although the statistics is not large, one sees an accumulation of events around $|\eta| = 1$, the region of the vertical crack between the barrel and extended barrel calorimeters, which results from the deterioration of the jet energy resolution in that region. There is also some accumulation of events around $|\eta| = 0$, where the deterioration of the resolution comes likely from the fact that particles from the jets are parallel to the orientation of the scintillator tiles of the tile barrel calorimeter. In this configuration, the sampling fraction of the calorimeter is less uniform.

The resolution $\sigma(p_{xy}^{miss})$ has been studied as a function of the total sum of transverse energy in the calorimeter (ΣE_T). In addition to the sample of Z+jet(s) events with $p_T^Z > 200$ GeV, a second sample of 4 554 events with $p_T^Z > 40$ GeV has been used. The $\sigma(p_{xy}^{calo})$ is reconstructed in the calorimeter and is compared to $\sigma(p_{x,y}^{\mu})$, the p_T components of the two muons from the Z decay. In this case, the muon momentum is reconstructed in the Muon System and no cut to reject radiative muons has been applied. Since there is no true E_T^{miss} in these events, except for the few events that may contain a neutrino, the two components $p_{x,y}^{calo}$ and $p_{x,y}^{\mu}$ should be equal and opposite and the distribution of their difference can be fitted by a Gaussian whose sigma gives the resolution on the measurement of the components of the E_T^{miss} vector in the event. The values of sigma are shown in Figure 9-40 as a function of the total transverse energy in the calorimeter, taken as the sum of the transverse energy of the reconstructed jets. The resolution is shown for the full simulation and ATLFAST.

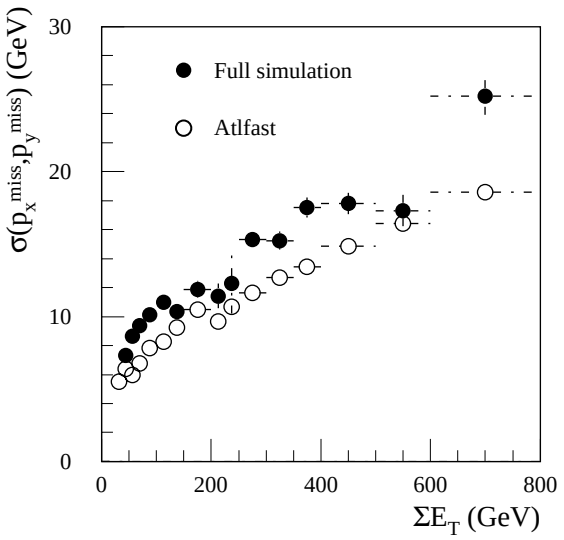

Figure 9-40 $\sigma(p_{xy}^{miss})$ as a function of ΣE_T in the calorimeter for Z+jet(s) events: detector resolution and physics effects are included (see text). Black dots are for full simulation and open dots for ATLFAST.

The full simulation gives a resolution about 20% worse than ATLFAST. The range of energies of the jets that are contributing to this sample is very large: from 20 GeV to about 800 GeV. In the full simulation, the E_T^{miss} is calculated from the sum of the energy of all cells of the calorimeters, applying to each calorimeter a single constant factor that corrects on average for the effect of the non-compensation of the calorimeter. These coefficients have been fitted to minimise the resolution for the overall sample. In ATLFAST, the $p_{x,y}^{calo}$ is calculated from the energy of the reconstructed jets at particle level (cone $\Delta R = 0.4$) smeared with a resolution given by $\sigma/E = 50\%/\sqrt{E} \oplus 3\%$, where cells unused in clusters are also taken into account. As was seen in Section 9.1.1, the best jet energy resolution is obtained when the calibration coefficients de-

pend on the jet energy and pseudorapidity and when correction terms taking into account the energy loss in dead material are added. Therefore the resolution obtained here with the simple algorithm used in this study is not optimum.

The resolution presented in Figure 9-40 is larger than the experimental resolution $\sigma(p_{xy}{}^{\mathrm{miss}})$ given in Section 9.2.1.6 which is fitted by the form: $\sigma(p_{xy}^{\mathrm{miss}}) = 0.46 \times \sqrt{\Sigma E_T}$. There are various effects that contribute to this difference. The above expression includes the detector energy resolution and the effect of the limited calorimeter coverage, since it is obtained by comparing the reconstructed p_{T} in the calorimeter to the sum of the p_{T} of all the particles without restriction in pseudorapidity, but does not include the fluctuation of the fragmentation process that contributes to the overall p_{T} balance of the event which is shown here. For example, the rms of the sum of the p_{T} of the particles resulting from the fragmentation of a 200 GeV quark (resp. 1000 GeV) at $|\eta| = 0.3$ is 5.5 GeV (resp. 16 GeV). In addition, in the sample of events considered here, the transverse energy measured in the calorimeter is deposited essentially by a single high-p_{T} jet. In that case, the contribution of the constant term of the jet energy resolution is important. When an equivalent amount of transverse energy is deposited by various jets, the most common physics case, then the resolution is dominated by the statistical term. This can be illustrated by a simple example: if n jets share equally the total energy E, then the energy resolution of each individual jet is $\sigma_{jet} = 50\% \times \sqrt{E/n} \oplus 3\% \times E/n$ and the total energy resolution is $\sigma_{tot} = 50\% \times \sqrt{E} \oplus 3\% \times E/\sqrt{n}$.

In this section it has been shown that no large $E_{\mathrm{T}}{}^{\mathrm{miss}}$ tail is produced by badly reconstructed jets in the less uniform sections of the hadronic calorimetry. In addition, to obtain the best $E_{\mathrm{T}}{}^{\mathrm{miss}}$ resolution, especially when a large range of jet energies is involved in a process of interest, one should apply an algorithm that adjusts the weights according to the jet energy and pseudorapidity and adds correction terms for energy loss in dead material.

9.3 Mass reconstruction

In this Section, the reconstruction of the mass of objects decaying to jets is discussed: the cases considered are $W \rightarrow jj$, $H \rightarrow b\bar{b}$, $Z \rightarrow \tau\tau$ and $H/A \rightarrow \tau\tau$, and $t\bar{t}$ final states.

9.3.1 $W \rightarrow jj$

The reconstruction of two jets coming from the hadronic decay of W bosons will play an important role in many physics signals at the LHC. These signals include: the search for SUSY, the search for a heavy Higgs boson, the measurement of the top quark mass, and QCD studies. The resolution on the reconstructed mass is influenced by physics effects, such as jet fragmentation, jet overlap, final state radiation and minimum-bias events, and detector effects such as calorimeter response, hadronic shower size and electronic noise. The relative importance of the different effects, and hence the best reconstruction strategy, depends on the p_{T} range of the W decays considered, since low-p_{T} W bosons decay to well separated low-energy jets while in the case of high-p_{T} W decays, the two jets tend to overlap.

In this section, a study of the di-jet mass resolution, tails and efficiency for different ranges of p_{T} of the W is presented. The relative merits of different reconstruction algorithms are discussed and the detector effects for different luminosity scenarios are shown. More specific uses of

$W \rightarrow jj$ decays such as the measurement of the top mass or the use of the W mass constraint for *in situ* jet energy-scale calibration are treated separately in the section on the top mass measurement (see Section 18.1.3) and in the section on absolute energy scale (see Section 12.5.1.2).

Three typical ranges of p_T of the W are considered: the very low-p_T range (below 50 GeV), the mid-p_T range (100 to 200 GeV) from W+jet, WZ or top production, and the high-p_T range (200-700 GeV) from heavy Higgs (m_H = 1 TeV) decays. Three different methods have been considered:

- Method 1: the mass is calculated from the four-momenta of the two massless jets.
- Method 2: the mass is calculated from the four-momentum of each calorimeter tower (m_{tower}=0) inside the two jets.
- Method 3: same as Method 2 but the energy is collected in a single cone to treat decays with severe overlap.

9.3.1.1 Low-p_T range

For the decays of low-p_T W's (see [9-23] for details) methods 1 and 2 have been applied using a fixed cone algorithm with ΔR = 0.4. Figure 9-41 shows the reconstructed mass spectrum for W bosons. These events were fully simulated. A simple calibration of the jet energy was done by multiplying the reconstructed energy by the average ratio of the parton energies to the jet energies. This needs to be done on a case-by-case basis, depending on the reconstruction method, the cone size and whether pile-up was included. The two jets in this sample are very well separated. The average angular distance ΔR is 3, and the resolution on the reconstructed W mass is dominated by the jet energy resolution. The resolution, resulting from a $\pm 2\sigma$ Gaussian fit, is 9.5 GeV without pile-up and 13.8 GeV with pile-up (applying a 1 GeV E_T tower cut) for W decays to jets with p_T greater than 25 GeV. The reconstructed mass is compatible with the generated value of m_W = 80.5 GeV. The addition of the pile-up did not bias the reconstructed mass for method 1 and shifted it down by about 2 GeV for method 2.

9.3.1.2 Mid-p_T range

W bosons from WZ and W+jet production have been used to study W's with p_T above 100 GeV, with an average value of the order of 120–150 GeV (see [9-23] and [9-15]). The angular distance ΔR between the two partons from W decays in the W+jet events is shown in Figure 9-17. The average jet angular distance of the WZ sample is slightly lower (1.3) than the one of the W+jet sample (1.6).

Methods 1 and 2 (see [9-23]) were applied to the WZ sample using a fixed cone algorithm with ΔR = 0.4. The data were fully simulated and the jet energy calibrated as described in Section 9.3.1.1. The results are shown in Figure 9-42. The two methods show a similar shape for the mass spectrum: there is a Gaussian component but a low-mass tail appears. The Gaussian part comes from the resolution of the jet energy. The tail appears for the events with a small opening angle between the jets, for ΔR between 0.5 and 1. The tail comes from a bias in the angle between the jets. This can be verified by calculating the mass from the reconstructed jet energies but using the true angle between the partons instead of the reconstructed angle. In that case, the low-mass tail disappears but not when the true quark energy is used together with the reconstructed angle. Even though a cone size ΔR = 0.4 was used, energy from one jet is included in the other, inducing a bias in the direction. The average reconstructed mass is (80.7 ± 0.4) GeV for

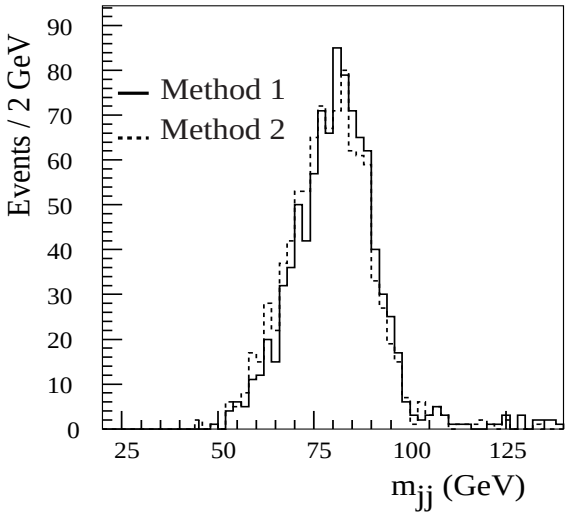

Figure 9-41 Reconstructed mass for low-p_T W's: full line shows method 1 (jet four-vector), and the dashed line shows method 2 (tower four-vector).

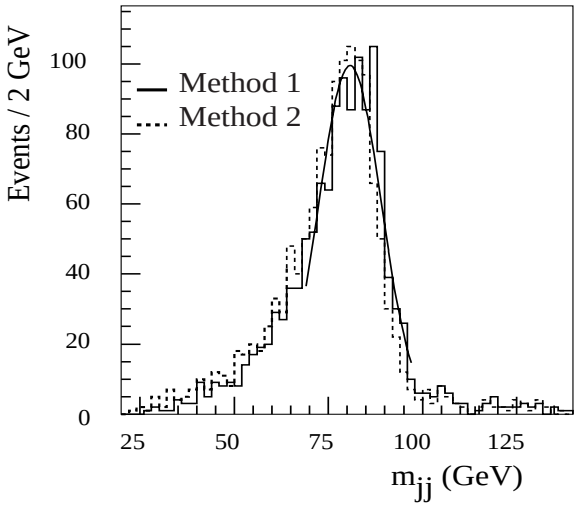

Figure 9-42 Reconstructed mass for mid-p_T W's: full line shows method 1 (jet four-vector), and the dashed line shows method 2 (tower four-vector).

method 1 and (79.5 ± 0.2) GeV for method 2 while the resolution is (7.7 ± 0.3) GeV and (8.3 ± 0.4) GeV, respectively. The addition of pile-up worsens the resolution to (12.9 ± 0.4) GeV even when increasing the cut on the jet transverse energy to 30 GeV.

The performance of method 1 with various jet algorithms has been tested on the sample of W+jet events with ATLFAST [9-15]. In this case, the particle-level energy of the reconstructed jet was used (no average calibration factor to the parton energy scale was applied). The comparison was made for the following algorithms: the conventional fixed cone jet algorithm for two cone sizes ΔR = 0.7 and 0.4, the K_T clustering algorithm (with the distance parameter used to stop cell merging set to R_{cut} = 0.4 [9-14],[9-10]), the MGS algorithm (with the two-jet separation parameter ΔR set to 0.3 [9-15]).

Figure 9-43 shows the result for the low-luminosity scenario. The cone method with ΔR = 0.7 gives the best performance: the average reconstructed mass is 78 GeV. The K_T and MGS algorithms reconstruct a mass average 3 GeV lower. For the cone method with ΔR = 0.4, the average reconstructed mass is even lower, 72.5 GeV.

Figure 9-44 shows the results for the high-luminosity scenario. The effect of minimum-bias events was simulated by adding an average of 50 minimum bias events generated with PYTHIA (with Poisson fluctuations) and simulated by ATLFAST. The events were added at the level of the projected E_T ($\Delta\eta \times \Delta\phi$) matrix. A cut of 2 GeV E_T was applied to the towers to limit the pile-up effect. In this case, the performance of the cone method with ΔR = 0.7 was seriously deteriorated, while the cone method with ΔR = 0.4, the K_T and MGS algorithms showed similar performance: the addition of pile-up contributed about 10 GeV (in quadrature) to the resolution, as observed also in the fully simulated WZ sample. On the other hand, the average reconstructed mass increased by 6.5 GeV for the cone method with ΔR = 0.4, 7 GeV for the K_T algorithm and 6 GeV for the MGS algorithm.

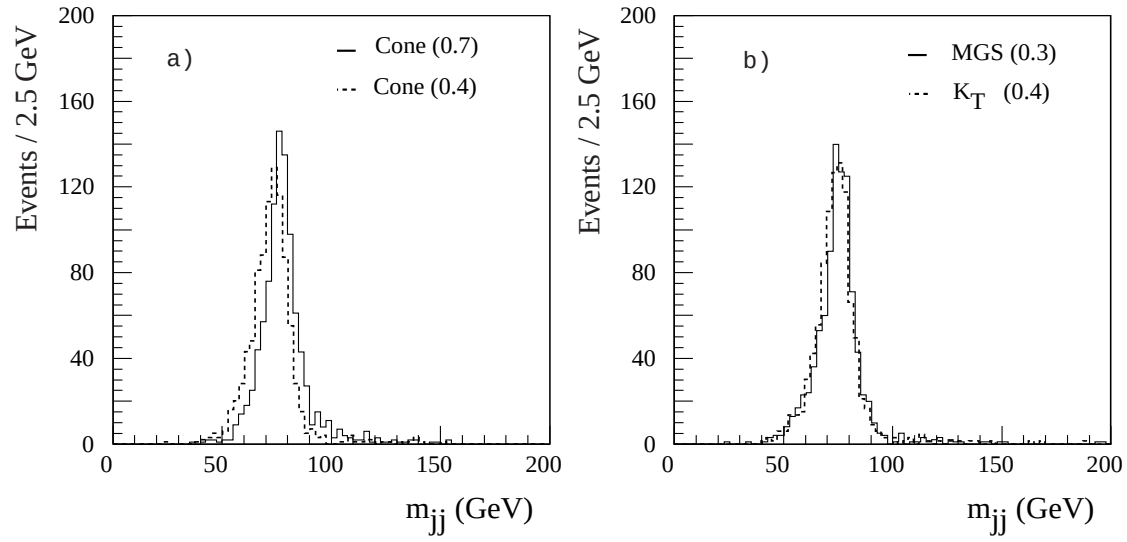

Figure 9-43 Reconstructed *W* mass without pile-up events for the *W*+jet sample: a) fixed cone algorithm with cone sizes $\Delta R = 0.7$ (average $m_W = 78$ GeV) and $\Delta R = 0.4$ (average $m_W = 72.5$ GeV); b) the K_T algorithm (average $m_W = 75$ GeV) and the MGS algorithm (average $m_W = 75$ GeV).

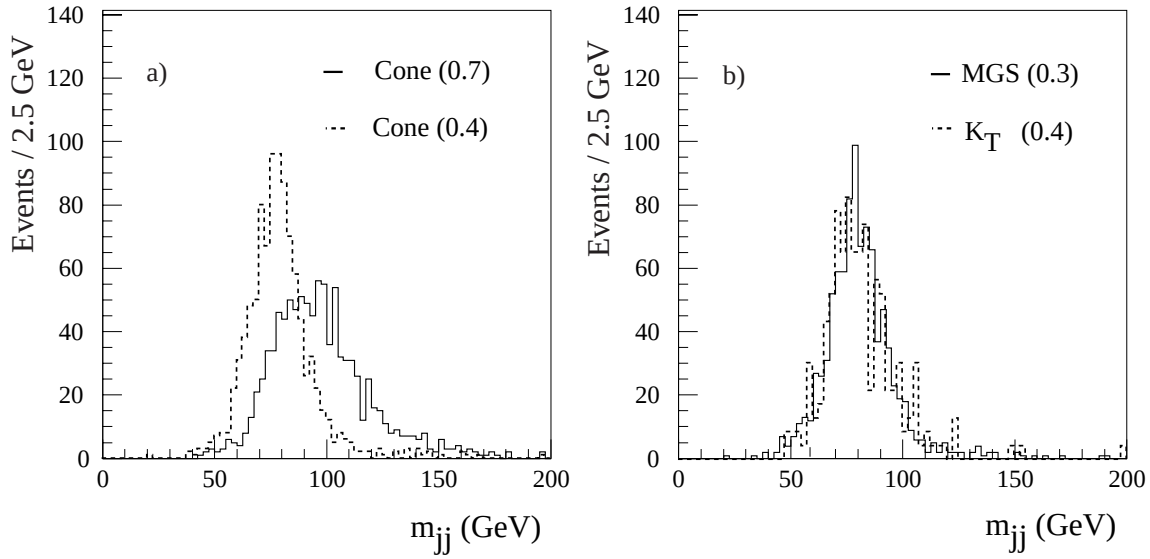

Figure 9-44 Reconstructed *W* mass with pile-up events added to the *W*+jet sample and with an E_T tower cut of 2 GeV: a) fixed cone algorithm with cone size $\Delta R = 0.7$ (full line) and fixed cone with $\Delta R = 0.4$ (dashed line); b) MGS algorithm (full line) and K_T algorithm (dashed line).

9.3.1.3 High-p_T range

The search for a heavy Higgs boson ($m_H > 600$ GeV) in the decay channel $H \rightarrow WW \rightarrow l\nu jj$ is one of the cases where an efficient reconstruction of high-p_T W's will be essential ([9-16],[9-17]). The separation in $\eta \times \phi$ for the case of a 1 TeV Higgs boson, is shown in Figure 9-45. Due to the boost, the two jets can be very close and will overlap. The range of E_T^{parton} studied in this fully simulated sample extends from 20 to about 500 GeV.

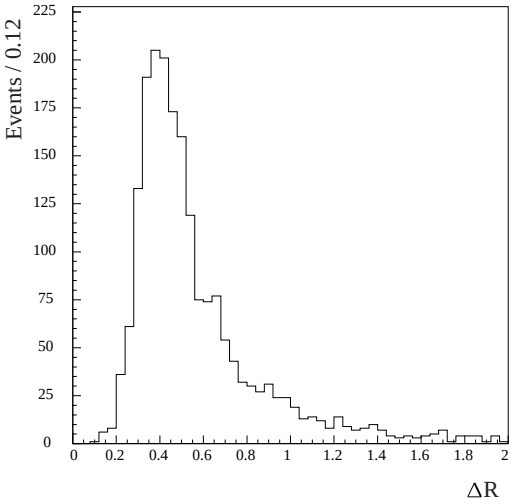

Figure 9-45 Distance ΔR between the two quarks from the WW decay of a 1 TeV Higgs.

In the case of method 1, where the W mass is reconstructed from the four-momenta of the two jets, the fixed cone algorithm has to be applied with a narrow cone in order to be efficient at separating the two jets. In this case the energy inside the cone tends to under-estimate the parton energy and the resolution deteriorates.

The results obtained with method 1 for various jet algorithms are shown in Figure 9-46 for the high-luminosity scenario with a 2 GeV cut on the tower E_T. In this particle level study, the energy of the jet is taken from the reconstructed particle-level jet energy. No additional calibration factor to equalise the jet energy to the parton energy was applied. In the case of the standard

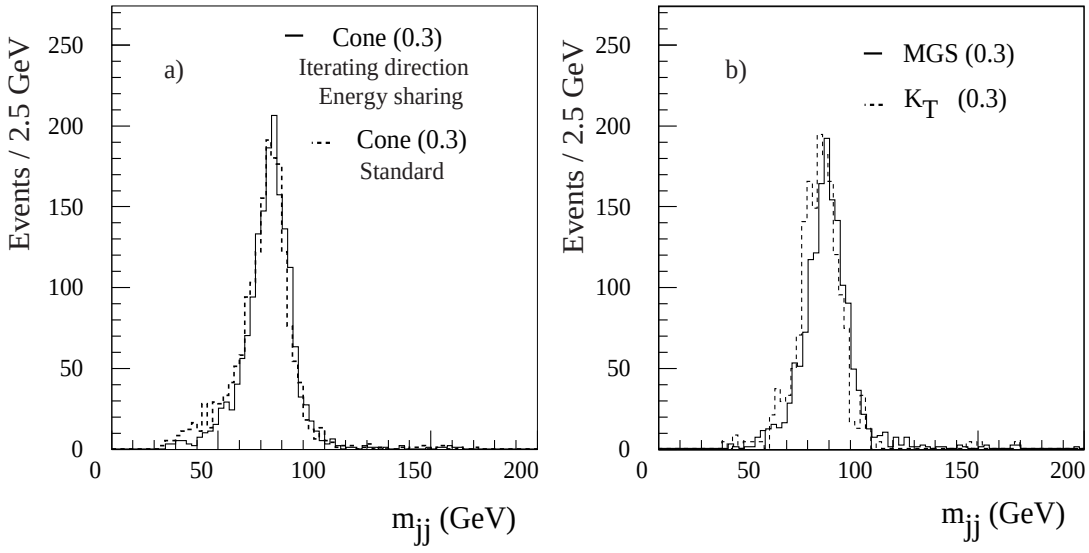

Figure 9-46 Reconstructed W mass with pile-up events for the 1 TeV Higgs boson sample, with an E_T tower cut of 2 GeV: a) cone algorithm with cone size $\Delta R = 0.3$ but iterating direction and jet energy sharing (an option of the MGS algorithm (full line), standard fixed cone algorithm with cone size $\Delta R = 0.3$ (dashed line); b) MGS algorithm (resolution = 0.3, full line), K_T algorithm ($R_{cut} = 0.3$, dashed line).

fixed cone algorithm, a low energy tail can be seen, due to the bias in the angle in the case of jet overlap. The tail can be reduced and the resolution improved by iterating the jet direction, resulting in the energy being shared between the two jets without biasing the jet that is reconstructed first, as happens in the standard cone algorithm. The low energy tail is further reduced in the case of the K_T and MGS algorithms with variable jet size but at the cost of some loss of efficiency.

When there is severe overlap between the jets, method 2 and method 3 may be more efficient. This follows since they have the advantage that very narrow initial cones (ΔR = 0.2) can be used to find the jet direction and that no energy sharing is needed, only the list of towers to be considered has to be known.

The performance of methods 1 and 2 has been studied with a sample of fully simulated heavy Higgs events. In this case, the reconstructed jet energies in the calorimeter are calibrated by multiplying by a constant factor taken as the average ratio of the parton energy to the reconstructed jet energy. The mass scale (defined as the ratio of the reconstructed W mass divided by the generated mass) is shown in Figure 9-47 as a function of the p_T of the W. The mass scale is divided, on an event-by-event basis, by the jet energy scale (the ratio of the reconstructed jet energy divided by the parton energy). In the case of method 1, a narrow ΔR = 0.2 cone has been used to determine first the jet barycentres. A cone of ΔR = 0.4 is then used to evaluate the jet energies; jet energy sharing is done by attributing the energy from a cell in the overlap region to the closest jet. The ratio of the mass scale to the jet energy scale is of the order of 0.95 and decreases slightly as a function of the p_T of the W, about 2% between 250 and 700 GeV. When the jets overlap, energy from one

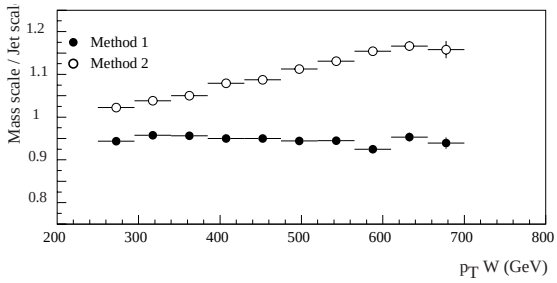

Figure 9-47 The ratio of the mass scale to the jet energy scale as a function of p_T^W for method 1 and method 2 (see text).

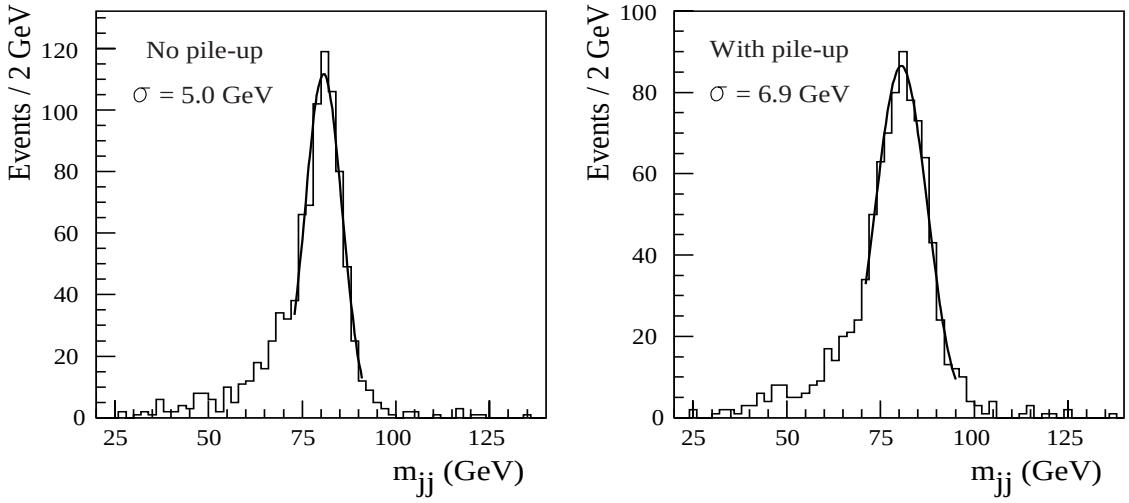

Figure 9-48 Reconstructed W mass using Method 2 after applying a linear correction as a function of the p_T of the W at low luminosity (left) and with high luminosity pile-up included (right)

jet gets included in the other one and result in the centres being too close which lowers the reconstructed mass. For method 2 (the same is true for method 3), the ratio of mass scale to jet energy scale is larger than one and increases significantly with the p_T of the W. This results from the following effect: when a particle points to a tower, it deposits its energy not only in that tower but also in the neighbouring towers because of the lateral shower size. When the mass is calculated, the energy is weighted according to the relative angle of each tower. Instead of all the energy of a particle being assigned to the tower that was hit, part of it is in the neighbouring towers. The overall effect is that the mass gets larger as shower size effects become more important. The W mass spectrum reconstructed with method 2 is shown in Figure 9-48 at low and high luminosity. A linear correction as a function of the p_T of the W has been applied to the mass to correct for the systematic bias mentioned above. The reconstructed mass is 80.5 GeV and the resolution is 5.0 GeV (6.9 GeV) at low (high) luminosity.

9.3.1.4 Conclusions

Jets from low-p_T W boson decays are well separated and the mass resolution is dominated by the jet energy resolution. As the p_T of the W increases, the jets start to overlap and the resulting systematic effects on the reconstructed mass are very dependent on the reconstruction method used.

9.3.2 $H \rightarrow b\bar{b}$

WH production, followed by the decay $H \rightarrow b\bar{b}$, is a promising channel to observe a Higgs boson signal at the LHC, both in the context of the Standard Model and of the MSSM, if the Higgs mass is in the range 80–100 GeV. In addition, $h \rightarrow b\bar{b}$ decays are expected to be a clean signature of SUSY final states, since over a large region of the parameter space squarks and gluinos include the h boson among the products of their cascade decays (Chapter 20). The reconstruction of the Higgs mass in the $b\bar{b}$ channel and the resulting mass resolution were studied by using fully-simulated events at low and high luminosity, and are discussed below. More details about this channel can be found in Section 19.2.4.

9.3.2.1 *WH* generation and selection

A sample of about 900 WH events, with $H \rightarrow b\bar{b}$ and $W \rightarrow l\nu$ ($l = e, \mu$), were generated with PYTHIA 5.7, including initial-state radiation, final-state radiation and hadronisation. The Higgs mass was chosen to be $m_H = 100$ GeV. Events were selected if the b-quarks satisfied $p_T > 15$ GeV and $|\eta| < 2.5$. The sample was then processed with the full-simulation chain.

In the following, a reconstructed jet was defined as a b-jet if its distance from a b-quark with $p_T > 5$ GeV (after final-state radiation) was $\Delta R < 0.2$. No b-tagging in the Inner Detector was required explicitly for the study presented here. This is not expected to bias the Higgs mass reconstruction as obtained from the calorimeters.

9.3.2.2 *WH* reconstruction at low luminosity

Jets were reconstructed with cones of size $\Delta R = 0.7$. The efficiency for reconstructing one or both b's produced in the Higgs boson decay is 83% and 69% respectively, where a b-jet is defined according to the criteria described in the previous section. Figure 9-49 shows the reconstructed in-

variant mass of the two *b*-jets for events where both *b*'s are reconstructed and both have $p_T > 15$ GeV. The jet energies were scaled by the average value of $K_{jet} = p_T^{parton} / p_T^{jet}$, where p_T^{parton} is the transverse momentum (before final state radiation) of the parton which initiated the jet. This correction factor decreases when p_T^{jet} increases and it becomes asymptotically equal to unity for $p_T^{jet} > 50$ GeV [9-24]. Before such a correction was applied, a large down-shift of the peak of the reconstructed two-jet mass was observed, which was mostly due to final-state radiation, hadronisation and the decay of the *b*-quarks: energy leaks outside the jet cone and the presence of neutrinos among the decay products are responsible for the degradation of the mass resolution and the appearance of low-energy tails. As a consequence, only 82% of the events are

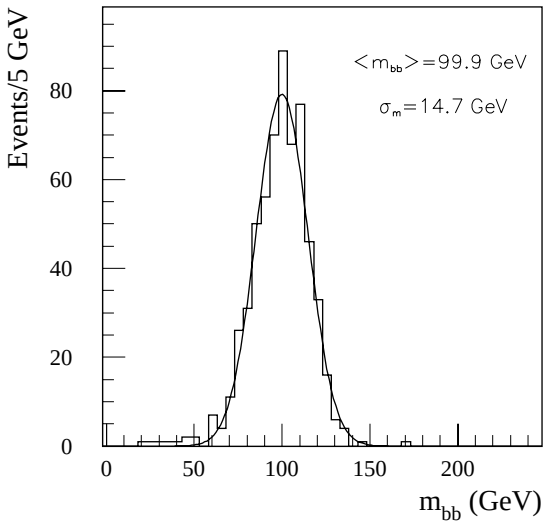

Figure 9-49 Reconstructed invariant mass distribution of the two *b*-jets in the final state for $H \to b\bar{b}$ events with m_H = 100 GeV at low luminosity.

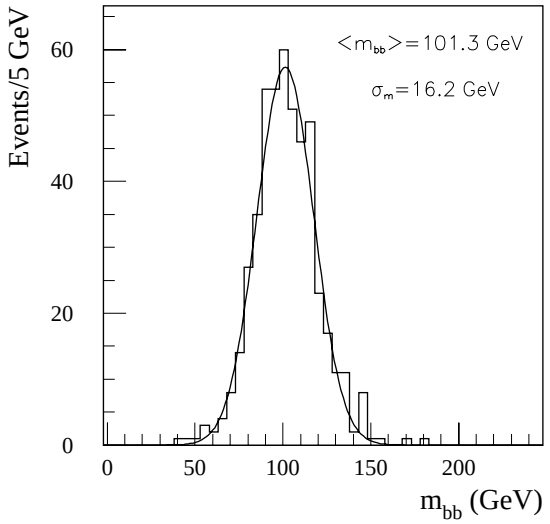

Figure 9-50 Reconstructed invariant mass distribution of the two *b*-jets in the final state for $H \to b\bar{b}$ events with m_H = 100 GeV at high luminosity.

contained inside a window of ±20 GeV around the peak of the distribution. After the calibration of the *b*-jet energy, the reconstructed mass peak is at the expected position, as it can be seen from Figure 9-49, and the mass resolution is ~15 GeV. This can be compared with a mass resolution of 12.8 GeV obtained with ATLFAST [9-24]. It should be noted that the *b*-jet scale will be calibrated *in situ* at the LHC by using for instance *Z*+jet events (see Section 12.5.1.3).

9.3.2.3 *WH* reconstruction at high luminosity

To study the *b*-jet reconstruction and mass resolution at high luminosity, pile-up was added to the signal sample in the way discussed in Chapter 2. Only calorimeter towers with a transverse energy content of larger than 1 GeV were used to reconstruct the jets. A jet cone size of $\Delta R = 0.4$ was chosen in this case in order to minimise the impact of pile-up. The *b*-jets were required to have $p_T > 15$ GeV and the jet energies were calibrated as described above. Figure 9-50 shows the reconstructed invariant mass distribution of the two *b*-jets at high luminosity. The mass resolution is 16 GeV and 80% of the events are contained in a window of ±20 GeV around the mass peak.

9.3.2.4 $H \rightarrow hh \rightarrow b\bar{b}b\bar{b}$

This channel was studied to assess the capability of reconstructing final states where more than one resonance decaying to jets is produced [9-25]. A high-statistics sample of fully-simulated $H \rightarrow hh \rightarrow b\bar{b}b\bar{b}$ events with m_H = 300 GeV and m_h = 80 GeV was used. Pile-up and electronic noise were not included.

Jets were defined as *b*-jets according to the criteria discussed in Section 9.3.2.1. Firstly, both $h \rightarrow b\bar{b}$ decays were reconstructed by assuming that the *h* boson has been discovered already and therefore its mass is known. This was used as a constraint to find the optimum combination of the four *b*-jets into two pairs, and therefore to reduce the combinatorial background. The chosen combination was the one which minimised $\chi^2 = (m_{b\bar{b}} - m_h)^2 + (m_{b\bar{b}} - m_h)^2$. The resulting $h \rightarrow b\bar{b}$ mass resolution was found to be 11 GeV for m_h = 80 GeV, with an event acceptance of 89% inside a mass window of $\pm 2\sigma_m$ around the peak. After selecting events where both $b\bar{b}$ masses are inside the above-mentioned mass window, the *b*-jet four-momenta were recalibrated by applying the constraint $m_{b\bar{b}} = m_h$. Finally, the four *b*-jet mass distribution was reconstructed (Figure 9-51). The resulting *H* mass resolution was about 13 GeV, with ~82% of the events inside a mass window of $\pm 2\sigma_m$.

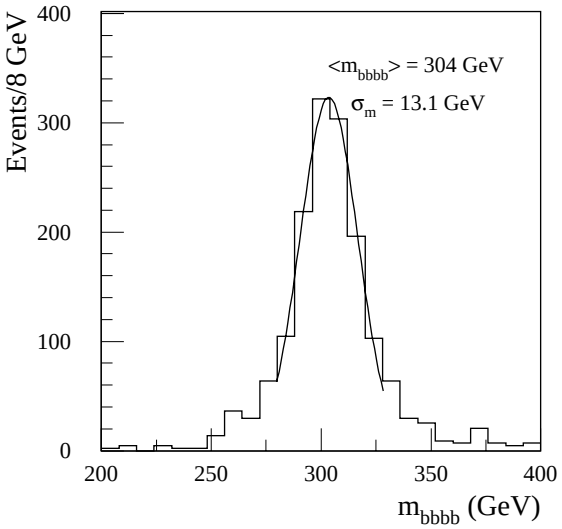

Figure 9-51 Reconstructed four *b*-jet mass spectrum for $H \rightarrow hh \rightarrow b\bar{b}b\bar{b}$ with m_H = 300 GeV.

9.3.3 $\tau\tau$ final states

In this section, the reconstruction of heavy particles decaying into τ pairs, with one τ decaying hadronically and the other one leptonically, is discussed. Such final states are expected for instance from the possible production and decay of the supersymmetric Higgs bosons *A* and *H*. Two methods to reconstruct the $\tau\tau$ invariant mass, one based on all products from τ decays and one on the visible decay products only, are presented.

The section starts with a discussion of $Z \rightarrow \tau\tau \rightarrow$ jet+lepton events, which could be used as a control sample for $\tau\tau$ final states. Indeed this sample would allow tests of the methods used to reconstruct the $\tau\tau$ invariant mass, and checks of the overall calorimeter calibration since the $\tau\tau$ invariant mass is obtained from several different objects (leptons, hadrons, missing transverse energy). Furthermore, the possibility of using these events for a precise measurements of the τ lifetime is briefly described. Finally, the reconstruction of $H/A \rightarrow \tau\tau$ events, and the performance in terms of mass resolution and acceptance in the mass bin, are discussed.

9.3.3.1 $Z \rightarrow \tau\tau$ reconstruction from all decay products

Fully-simulated samples of $Z \rightarrow \tau\tau \rightarrow$ jet+lepton events and of the main backgrounds were used for the study presented here, together with a sample of events simulated with ATLFAST.

The invariant mass of the τ-pair produced in the decay of a Z boson, or of any other particle, in the channel

$$Z \rightarrow \tau\tau \rightarrow \text{jet } \nu_\tau \; l\nu_l\nu_\tau$$

can be reconstructed under the assumptions that $m_\tau = 0$, that the direction of the neutrino system from each τ decay ($\bar{\nu}_1 = \bar{\nu}_\tau$, $\bar{\nu}_2 = \bar{\nu}_l + \bar{\nu}_\tau$) coincides with that of the detected products of the τ decay, and that the τ decay products are not back-to-back.

The reconstructed mass is then given by

$$m_{\tau\tau} = \sqrt{2(E_1 + E_{\nu 1})(E_2 + E_{\nu 2})(1 - \cos\theta)}$$

where E_1 and E_2 are the energies of the detected products from the τ decay, $E_{\nu 1}$ and $E_{\nu 2}$ are the energies of the two neutrino systems, and θ is the angle between the directions of the detected products. $E_{\nu 1}$ and $E_{\nu 2}$ are obtained by solving the system

$$p_x^{\text{miss}}(p_y^{\text{miss}}) = (E_{\nu 1}\bar{u}_1)_{x(y)} + (E_{\nu 2}\bar{u}_2)_{x(y)}$$

where $\bar{u}_1$ and $\bar{u}_2$ are the directions of the detected products, and p_x^{miss} and p_y^{miss} are the two components of the $E_{\text{T}}^{\text{miss}}$ vector. This system can be solved if the determinant, sin Δφ, is not zero, where Δφ is the azimuthal angle between the jet and the lepton produced in the τ decay. The kinematics of the event, the accuracy in the measurement of p_x^{miss} and p_y^{miss} in the calorimeter, and the assumption made on the particle directions contribute to the width of the reconstructed mass and can result in unphysical negative solutions for $E_{\nu 1}$ and $E_{\nu 2}$. In this case, the Z mass cannot be reconstructed. The mass resolution obtained in this way is proportional to $\sigma(E_{\text{T}}^{\text{miss}}) / |\sin\Delta\phi|$, therefore both the $E_{\text{T}}^{\text{miss}}$ resolution and the azimuthal separation between the lepton and the jet are important in the mass reconstruction. The variable Δφ depends on the p_{T} of the parent particle (*e.g.* a Z), and it is concentrated around π if the p_{T} is small, as shown in Figure 9-52. The dependence of the reconstructed ττ mass on Δφ is illustrated in Figure 9-53 in the case of Z production and decay; if Δφ is close to π (back-to-back events), the neutrino system yields bad solutions giving rise to tails at high values of the reconstructed mass.

Table 9-8 shows the mean value and the sigma of the ττ invariant mass distribution for $Z \rightarrow \tau\tau$ decays, together with the fraction of events lost in the individual selections of the mass reconstruction procedure. All events were used at this level, without applying any cuts, and a 100% τ identification efficiency is assumed. Therefore, event losses were due to cases where the above-mentioned system of equations yielded unphysical solutions for the neutrino energies. Starting from the mass distribution as generated by PYTHIA (first step), four other steps were considered. In the second step, $m_{\tau\tau}$ was reconstructed by using the particle level information, that is using the generated energies and directions. In particular, the components of the $E_{\text{T}}^{\text{miss}}$ vector were calculated without any restriction on the pseudorapidity coverage of the detector. At this stage, the event loss and the deterioration of the mass resolution were due to the assumption on the directions of the τ decay products. In the third step, the reconstructed mass was obtained in the same way as in the second step but using a cut $|\eta| < 5$ for the $E_{\text{T}}^{\text{miss}}$ reconstruction. The resulting event loss and deterioration of the mass reconstruction were due to the limited pseudorapidity coverage of the detector. In the fourth step, p_x^{miss} and p_y^{miss} as obtained from full simulation were used. The deterioration of the performance was due to the $E_{\text{T}}^{\text{miss}}$ experimental resolution. Finally, in the fifth step, the reconstructed energies and directions of the jet and the lepton were used. It can be seen that the event losses and the deterioration of the mass reconstruction and resolution are mainly due to the assumption on the particle directions, to the limited pseudorapidity coverage of the detector and to the $E_{\text{T}}^{\text{miss}}$ resolution.

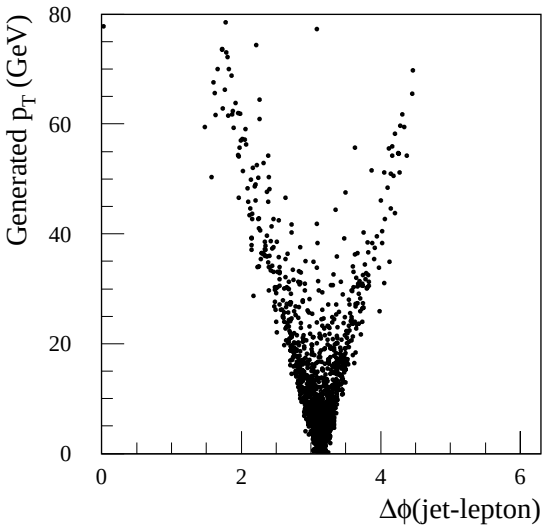

Figure 9-52 The azimuthal angle between the jet and the lepton produced in the decay of the two τ's as a function of the generated p_T of the Z.

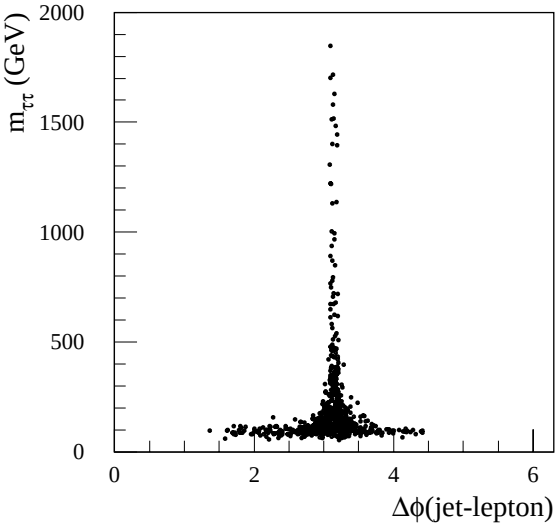

Figure 9-53 The reconstructed $Z \rightarrow \tau\tau$ mass as a function of the azimuthal angle between the jet and the lepton produced in the decay of the two τ's.

Table 9-8 For $Z \rightarrow \tau\tau$ decays, the mean value and the σ of the reconstructed mass spectrum, and the fraction of events lost, as a function of the selection in the reconstruction procedure (see text).

Selection	$<m_{\tau\tau}>$ (GeV)	σ ($m_{\tau\tau}$) (GeV)	Lost events
Generation level	91.2	1.7	0
Particle level	92.0.	7.4	28%
Particle level $\|\eta\| < 5$	97.0	12.0	46%
E_T^{miss} from full simulation	97.6	15.3	52%
Reconstructed jets and leptons	98.7	15.8	52%

An analysis similar to that used to select final states due to the production and decay of the A boson (Chapter 19) was performed to extract a clean sample of Z events, with a well reconstructed mass, from the main backgrounds (W+jets and $b\bar{b}$ production). The following cuts were used for this purpose:

- The τ-jet should be identified according to the criteria described in Section 9.1.5.
- $p_T^{jet} > 30$ GeV, $|\eta|_{jet} < 2.5$.
- $p_T^{lepton} > 16$ GeV and $|\eta|_{lepton} < 2.5$ for the lepton produced in the leptonic τ decay.
- No tagged b-jet in the event.
- Transverse mass m_T (lepton-E_T^{miss}) < 50 GeV.
- $1.8 < \Delta\phi < 2.7$ or $3.6 < \Delta\phi < 4.5$.
- 66 GeV < $m_{\tau\tau}$ < 116 GeV.

Table 9-9 Production cross-section, acceptance and expected number of events with an integrated luminosity of 10 fb^{-1} for the $Z \rightarrow \tau\tau$ signal and the main backgrounds.

	$Z \rightarrow \tau\tau$	$b\bar{b}$	W+jets
σ (nb)	1.5	19.9 ($p_T^{\mu} > 16$ GeV)	392 ($p_T^{\mu} > 16$ GeV)
Acceptance	4.8x10^{-4}	3x10^{-6}	1.3x10^{-6}
Events in 66-116 GeV	3500	270	500

About 3 500 signal events satisfying the above cuts are expected with 10 fb^{-1} of integrated luminosity. The background is about 20% (Table 9-9). The background can be further reduced by applying a more stringent cut on the transverse mass ($m_T < 25$ GeV), which removes W+jet events, and by introducing a cut on the missing transverse momentum ($E_T^{miss} > 18$ GeV), which rejects $b\bar{b}$ final states. With this set of cuts, the background in the mass window is reduced to ~6% and about 1 300 signal events are expected for 10 fb^{-1} of integrated luminosity. The reconstructed Z mass obtained in this way (Figure 9-54) is well centred at the nominal value and has a resolution of about 9 GeV.

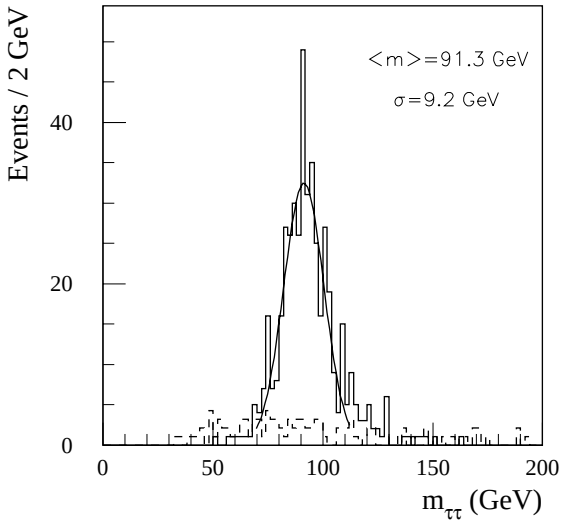

Figure 9-54 Reconstructed $Z \rightarrow \tau\tau$ mass spectrum at low luminosity. The dashed line indicates the background.

It should be noted that the results shown in the last row of Table 9-8 were obtained without applying any cuts. In particular the $\Delta\phi$ cut improves significantly both the mass resolution and the correct reconstruction of the mass peak.

9.3.3.2 $Z \rightarrow \tau\tau$ reconstruction from observed decay products

The reconstruction of the $\tau\tau$ invariant mass shown in the previous section relies on the assumption that the missing transverse energy in the event arises only from the neutrinos emitted in τ decays. There are cases where this is not true and yet the invariant mass of the $\tau\tau$ system is an important quantity. An example is given by the decays of supersymmetric particles in some models (see Chapter 20), where the measurement of the τ momentum and of the $\tau\tau$ invariant mass distribution would provide detailed information regarding the particle masses. In these cases, the $\tau\tau$ invariant mass must be reconstructed from the visible products of the τ decays only [9-26]. Missing transverse momentum and jet activity can be used as a trigger and event selection. The events so selected are rich in τ's, hence the primary background arises from jets in the same event and the τ identification criteria can be relaxed at the cost of lowering the rejection factor against jets. Leptonic τ decays are not useful, since the resulting electron or muon cannot be attributed to a τ decay, given the presence of other leptons in supersymmetry events. Hadronic τ decays must therefore be used.

In order to study how well this can be done, fully-simulated samples of Z+jet events were used. No pile-up was included, therefore the results are limited to the case of low luminosity. Separate samples were generated for different values of the 'Z mass' and for several ranges of transverse momenta. The rejection against jets was studied using the QCD jets in the same events.

Jets were reconstructed using a fixed-cone algorithm with a cone radius $\Delta R = 0.4$. A calorimetric isolation was applied by requiring that 96% of the energy be contained in the core of the jet, *i.e.* within $\Delta R = 0.2$ of the jet's centroid. This retained 74% of the hadronically decaying τ's and 17% of the jets. Additional jet rejection can be obtained by studying the mass of the jet, calculated by assuming that the energy in each calorimeter cell is due to a single massless particle at the centre of the cell. Requiring that this mass be less than 3.6 GeV reduced the acceptance to 65% (6.6%) for τ's (jets). This rejection against jets is sufficient to extract a supersymmetry signal.

In order to make an accurate reconstruction of the τ's, the Inner Detector was used to measure the momentum of charged tracks and the EM Calorimeter to measure the energy and hence the momentum of the photons that arise from π^0 decays. The xKalman package was used to reconstruct tracks in a road defined by the direction of the τ–jet candidate. These tracks were then extrapolated to the EM Calorimeter. Tracks reconstructed in this way can arise from τ decays, γ conversions or particles of the underlying event that happen to be nearby. Tracks of transverse momenta less than 1 GeV were not included to reduce the contamination. To reconstruct the mass of the τ-jet, all EM cells with $E_T > 1$ GeV were combined with the reconstructed charged tracks, which were all assumed to be pions. The Hadronic Calorimeter was not used. If a track deposits energy in a calorimeter cell, care must be taken to avoid overcounting. Assuming that the conversion electrons can be identified, the electromagnetic energy was included and the track dropped. For other tracks, the cell that was hit by the track was not included. The reconstructed jet mass showed the presence of a ρ peak, as expected from τ decay.

In events where two τ-jets were selected, the mass of the di-jet system was measured. This mass distribution showed a broad peak below the Z mass. The peak was sharpened by including only events where the reconstructed τ mass was greater than 0.8 GeV. This biased the sample against single-pion decays and in favour of decays where the energy carried by the neutrino was small. Table 9-10 shows the values of the reconstructed τ-pair mass and resolution obtained as a function of the generated mass. The ratio of the position of the peak to the generated mass is constant within errors and is independent of the transverse momentum of the produced particle (for $p_T < 125$ GeV).

The τ charge was determined as described in Section 9.1.5.1. These results on the efficiency, jet rejection, τ-pair mass resolution and charge identification are parametrised and used in the supersymmetry studies presented in Chapter 20.

9.3.3.3 τ lifetime measurement in $Z \rightarrow \tau\tau$ events

The current world average for the τ lifetime is 290.5 ± 1.0 fs [9-27]. Improvements in this measurement would be welcome in order to provide tests of the universality of the charged current and reduce the error on α_s. In this section, the results of a preliminary study to examine the ATLAS potential in the $Z \rightarrow \tau\tau$ channel are given.

$Z \rightarrow \tau\tau$ events were identified and reconstructed as described in Section 9.3.3.1, where one τ decaying to an electron or muon is used for triggering and the other τ decays hadronically. In order to measure the τ lifetime, three-prong decays were used to reconstruct the decay length ($c\tau = 87$ μm) in the Inner Detector.

Table 9-10 The reconstructed values of the peak of the ττ invariant mass as a function of the generated pair mass 'M_Z'**.** Also shown are the standard deviation and the ratios of the peak and of the standard deviation to the generated pair mass.

'M_Z' **(GeV)**	**Reconstructed** $M(\tau\tau)$ **(GeV)**	$\sigma(M)$ **(GeV)**	$M(\tau\tau)/M_Z$	$\sigma(M)/M_Z$
25	18.6	4.9	0.75	0.20
50	36.3	8.9	0.72	0.18
75	50.0	12.4	0.66	0.17
91	63.0	17.5	0.67	0.19
200	131.0	38.0	0.65	0.19

Reconstruction

Fully-simulated $Z \rightarrow \tau\tau \rightarrow$ jet+lepton events were used. To identify the events and reduce the backgrounds, it was required that the lepton should have $p_T > 24$ GeV, the jet $E_T > 30$ GeV and the reconstructed mass should be between 60 and 120 GeV. This resulted in an efficiency of 1.5%.

The direction of the jet was found from the calorimetry and a search was made in the ID in a cone of $\Delta R = 0.4$ around this direction. Jets were required to have at least two reconstructed tracks with $p_T > 2$ GeV satisfying the basic ID quality cuts Section 3.1.3. These tracks were used to reconstruct a secondary vertex using the algorithm described in Section 3.6. It was required that the vertex position should be within 2 cm of the beam spot in both *x* and *y*, that the net charge of reconstructed tracks associated with the displaced vertex should be ≤2 and that the invariant mass of these charged particles should be between 0.4 and 1.78 GeV. The efficiency to reconstruct at least two of the tracks was 87%, while the efficiency to reconstruct a vertex satisfying the cuts was 80%. The resolution of the vertex position in the transverse plane was 490 μm, corresponding to a resolution on the proper decay length of 17 μm.

To reconstruct the proper lifetime of the τ, it is necessary to boost back into the τ rest-frame with the Lorentz factor p_τ / m_τ, where p_τ is obtained from the p_T of the system recoiling against the *Z*, projected along the directions of the τ's. Equivalently, p_τ can be found from the missing energy, as explained in Section 9.3.3.1. A valid solution for the τ momentum was obtained in 52% of cases (see Table 9-8). The uncertainty in the determination of the recoil momentum leads directly to an uncertainty in p_τ and hence in the proper lifetime estimate. The statistical uncertainty on p_τ was typically 15%. It should be possible to control the systematic uncertainty by using $Z \rightarrow ee$ or $Z \rightarrow \mu\mu$ events with similar topologies to $Z \rightarrow \tau\tau$. For these events, the recoil measured by the calorimetry can be compared directly with the p_T of the *Z* measured by the leptons.

Lifetime estimate

The Inner Detector measures impact parameters of tracks with a resolution which is independent of momentum for particles with more than ~10 GeV. Hence the estimate of the proper decay length (rather than that measured in the laboratory frame) is fairly independent of the τ momentum. The statistical resolution on the proper decay length from the combination of the vertexing and the estimate of the τ momentum is of the order of 21 μm (corresponding to 55 fs). To estimate the statistical uncertainty on the τ lifetime τ_τ which could be achieved with *N* τ decays, a simple Monte Carlo study was made where the exponential proper lifetime distribution was

smeared with the statistical resolution and the lifetime was obtained using a likelihood method. The effective resolution provided by a single event is the sum of the measurement resolution (55 fs) and the lifetime (291 fs) combined in quadrature. Since the latter is quite a bit larger, it was found to dominate the error with the result that $\sigma(\tau_\tau) \approx \tau_\tau / \sqrt{N}$.

At the LHC, the cross-section for $Z \rightarrow \tau\tau$ will be 1.5 nb, with a branching ratio of 11% for a lepton and a three-prong hadronic decay. The reconstruction and selection described above results in an efficiency of 0.54%. If 30 fb^{-1} were collected in the low-luminosity phase, then 26 000 reconstructed τ's could be used, leading to a statistical error on the τ lifetime of 1.8 fs.

For an ATLAS measurement to be competitive, it will be necessary to have higher statistics, since improvements in the vertexing will not help significantly. This may occur from a larger integrated luminosity being delivered or from an increased efficiency. More work is needed to understand how the kinematical cuts could be loosened without increasing the errors resulting from the background. The cuts used in Section 9.3.3.1 give good background rejection but lead to efficiencies which are too small. *W*+jet events will be removed by the mass cuts, and apart from a small amount of gluon splitting to heavy flavour, the jets should not contain significant lifetime information, hence this background should not be a problem. The *B* lifetime is a factor of five larger than that of the τ, hence more care will be required with $b\bar{b}$ events. Nevertheless the background looks tolerable and should be significantly reduced by the kinematical cuts. In addition, further cuts on lepton isolation could be used.

Concerning systematic errors coming from the determination of the decay length in the ID, the average radial position of the detectors in the *B*-layer should be well determined using the constraints of the overlaps [9-28]. The aim is to understand the alignment in $R\phi$ to O(1) μm, which should be compared to the typical impact parameters which will be of the order of $c\tau_\tau$ = 87 μm. How this will contribute to the systematics of the lifetime needs to be studied and will depend on the exact nature of the alignment uncertainties; however, it is conceivable that many systematic contributions will cancel for the lifetime estimate.

9.3.3.4 $H/A \rightarrow \tau\tau$

The same method for reconstructing the $\tau\tau$ invariant mass as described for $Z \rightarrow \tau\tau$ final states in Section 9.3.3.1 was applied to $H/A \rightarrow \tau\tau$ decays. The fully-simulated sample of events from direct *A* production described in Section 9.1.5 was used for this study. The resulting τ-pair mass spectrum is shown in Figures 9-55 and 9-56 for m_A = 150 GeV and m_A = 450 GeV respectively.

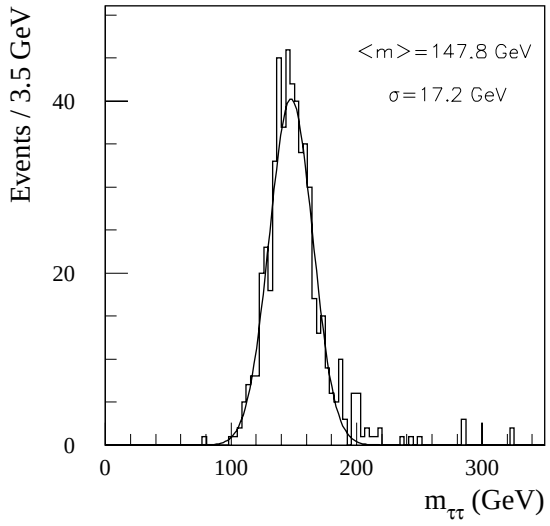

Figure 9-55 Reconstructed $A \rightarrow \tau\tau$ mass at low luminosity for m_A = 150 GeV.

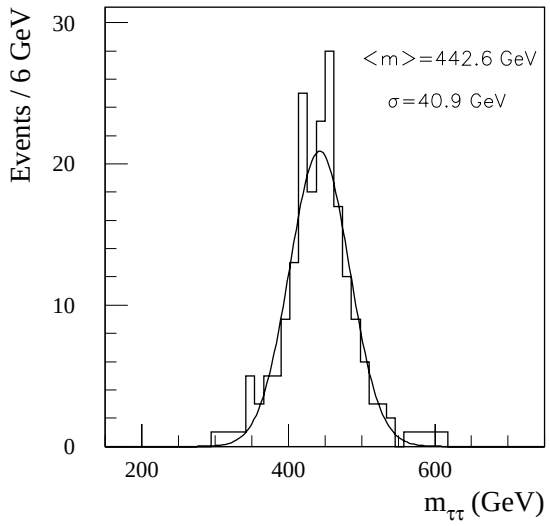

Figure 9-56 Reconstructed $A \rightarrow \tau\tau$ mass at low luminosity for m_A = 450 GeV.

Events with $2.9 < \Delta\phi < 3.4$, where $\Delta\phi$ is the azimuthal angle between the lepton and the jet from the τ decays, were rejected in order to improve the quality of the mass reconstruction. As already mentioned when discussing $Z \rightarrow \tau\tau$ decays, the reconstructed mass distribution has tails at high values. This is shown in Figure 9-57 for three different A masses. Comparing Figure 9-57 with Figure 9-53, it can be seen that the $\Delta\phi$ distribution is less peaked around π for A events than for Z events. This is due to the fact that the p_T of the A is in general larger than the p_T of the Z. As a consequence, the fraction of events lost because the system of equations giving the neutrino energies yields unphysical solutions is smaller than in the Z case, and decreases with increasing m_A (from ~40% for m_A = 150 GeV to ~25% for m_A = 450 GeV).

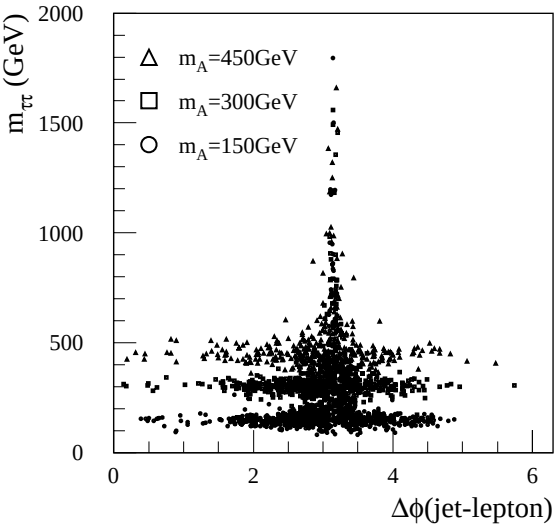

Figure 9-57 Reconstructed $A \rightarrow \tau\tau$ mass as a function of $\Delta\phi$ (jet-lepton) for m_A = 150, 300 and 450 GeV.

At low luminosity, a mass resolution in the range 20-40 GeV was obtained for A events with m_A = 150-450 GeV. If only events inside the mass window $m_A \pm 1.5\sigma(m_{\tau\tau})$ are accepted, the signal is reduced by a factor of two while the background by a factor of ten (Chapter 19).

At high luminosity, the pile-up has a large impact on the E_T^{miss} resolution and therefore on the A mass resolution. As mentioned in Section 9.2.1, a cut-off on the minimum transverse energy in each calorimeter tower was applied to improve the E_T^{miss} resolution. This cut affects the energy scale, therefore, prior to the mass reconstruction, the reconstructed τ-jet energy was corrected by a factor obtained by comparing the reconstructed and the generated τ-jet energy. The resulting mass spectrum is shown in Figure 9-58, and can be compared with the low-luminosity result in Figure 9-55. The tower cut-off (~1 GeV) which optimises the E_T^{miss} resolution was applied at high luminosity.

Figure 9-59 shows the ratio of the standard deviations of the reconstructed ττ mass spectrum at high luminosity and low luminosity, as a function of the tower E_T cut-off for m_A=150 GeV. For the optimum cut-off, this ratio is about two, so the selected mass window has to be enlarged at high luminosity to maintain good signal acceptance, at the expenses of a reduced background rejection.
The event acceptances in the mass window $m_A \pm 1.5\ \sigma(m_{\tau\tau})$ at low and high luminosity are compared in Figure 9-60. Although at high luminosity a mass bin twice as large as the mass bin at low luminosity was used, the signal acceptance was 60% of the acceptance at low luminosity. This is due to the fact that in the presence of pile-up, the fraction of events for which the neutrino system has unphysical solutions is larger.

.

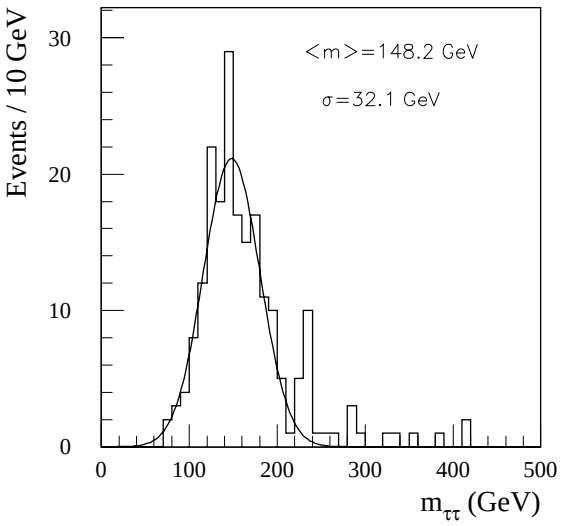

Figure 9-58 Reconstructed $A \rightarrow \tau\tau$ mass at high luminosity for m_A = 150 GeV and a tower cut-off E_T > 1 GeV.

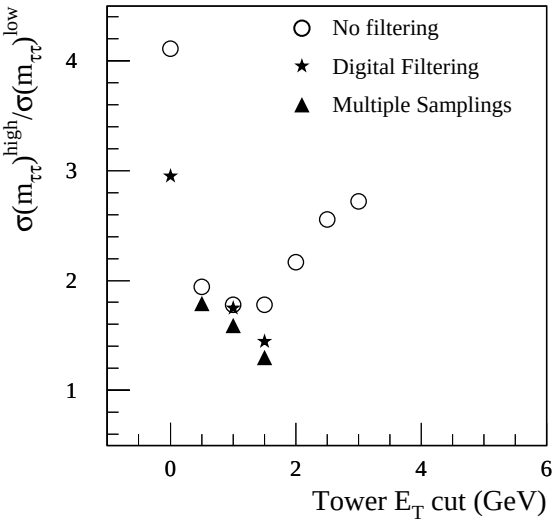

Figure 9-59 Ratio of the $A \rightarrow \tau\tau$ mass resolutions at high and low luminosity, for m_A = 150 GeV, as a function of the tower cut-off E_T, when no digital filtering is used (open circles), when digital filtering is used (stars), and when multiple sampling techniques are used (triangles).

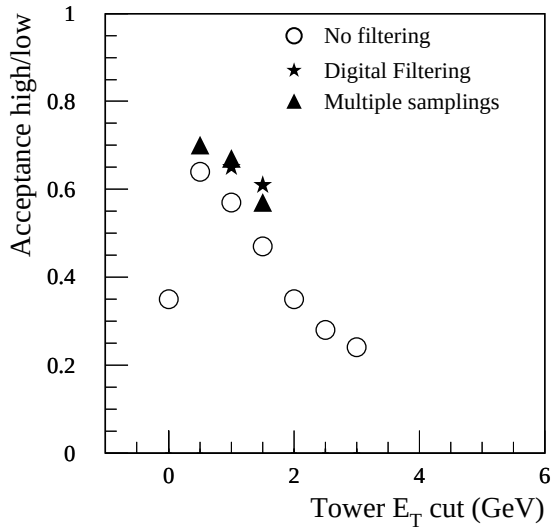

Figure 9-60 Ratio of the event acceptance in a mass window $m_A \pm 1.5\ \sigma(m_{\tau\tau})$ at high and low luminosity, for m_A = 150 GeV, as a function of the tower cut-off E_T. The symbols are as in Figure 9-59.

To minimise the effect of the pile-up, multiple-sampling and digital-filtering techniques for the calorimeter signals will be used. Preliminary results obtained by performing digital filtering or simple weighted combinations of multiple samplings look promising and show some improvement in the performance, as can be seen in Figures 9-59 and 9-60.

In conclusion, the impact of pile-up on the physics sensitivity is that the significance of a possible $H/A \rightarrow \tau\tau$ signal will most likely be a factor 1.5-2 smaller at high luminosity than it would be naively expected from the increase by a factor of ten in luminosity.

9.3.4 Top-quark final states

Reconstruction of final states containing top quarks is interesting for two reasons. Firstly, inclusive $t\bar{t}$ production will be used at the LHC to measure the top mass with high precision. Second, several channels from new physics (*e.g.* Higgs and SUSY) are expected to contain $t\bar{t}$ pairs produced in association with, or in the decay of, new particles. The reconstruction of events containing top quarks is challenging, because these events are characterised by a high multiplicity of jets, including *b*-jets, which often translates into a large combinatorial background. Good di-jet and multi-jet mass resolution is needed to reduce this background, and good calorimeter granularity is required to separate nearby jets.

The reconstruction of top final states is discussed here for two cases: the inclusive $t\bar{t}$ sample and the associated production $t\bar{t}H$ with $H \rightarrow b\bar{b}$. Both these channels were studied with full simulation and the results are presented in the next two sections. The impact of these results on physics is discussed in the relevant physics chapters (Chapter 18).

9.3.4.1 Inclusive $t\bar{t}$

The gold-plated channel for the measurement of the top mass at the LHC is the inclusive $t\bar{t}$ production, with one top decaying semileptonically ($t \rightarrow l\nu b$) and the other one hadronically ($t \rightarrow jjb$). In the method presented here, the top mass spectrum is extracted from the invariant mass distribution of the three-jet system arising from the hadronic top decay.

A sample of about 30000 fully-simulated $t\bar{t}$ events from inclusive production and with the above-mentioned decay modes were used for this study. Electronic noise and pile-up were not included. Jets were reconstructed by using the standard fixed-cone jet algorithm with a cone size $\Delta R = 0.4$, and their energies were calibrated by using the method described in Section 9.3.1.1. At least four jets with $p_{\mathrm{T}} > 40$ GeV and $|\eta| < 2.5$ were required, and at least two of the jets were required to be tagged as *b*-jets (according to the definition given in Section 9.3.2.1). For the accepted events, the decay $W \rightarrow jj$ was reconstructed by using those jets which were not tagged as *b*-jets. The average p_{T} of the W boson in this event sample was about 130 GeV, which is comparable to the case discussed in Section 9.3.1.2. The jet pair with an invariant mass m_{jj} closest to m_W was selected as the W candidate. The invariant mass distribution of the selected di-jet combinations is shown in Figure 9-61, and has a resolution of about 8 GeV (the resolution obtained with fast simulation was about 7.3 GeV). The event acceptance in a mass window of 20 GeV around m_W was 67%, and the contamination from the combinatorial background of order 10%. Other selection criteria, such as requiring that the highest-p_{T} jet be part of the combination, did not improve significantly the purity or efficiency, and therefore are not considered in the following. Events with $|m_{jj} - m_W| < 20$ GeV were retained, and the W candidate was then combined with the *b*-tagged jets to reconstruct $t \rightarrow jjb$. If no further restriction is applied, at least two *jjb* combinations are reconstructed in each event. In this case, the right combination is always selected but the purity of the sample is only 30%. To improve the purity, a variety of criteria were tried, including choosing the *jjb* combination which gave the highest p_{T} of the reconstructed top candidate, or using the *b*-jet which was furthest from the isolated lepton. Similar results were obtained for these various methods. Figure 9-62 presents the reconstructed

m_{jjb} distribution obtained by using the *jjb* combination which gives the highest p_T of the reconstructed top. Fitting the distribution with a Gaussian plus a third-order polynomial yielded a top mass consistent with the generated value of 175 GeV, and a m_{jjb} mass resolution of about 13 GeV. The resolution obtained with fast simulation was 11.4 GeV.

The total acceptance of the selection cuts described above was 5.7%, with a contamination from the combinatorial background from the signal itself of about 20%. These numbers include the event acceptance in the top mass window 175 ± 35 GeV, and are in good agreement with the results found with fast simulation. More details about the top-mass reconstruction, as well as a discussion of the top-mass measurement, can be found in Chapter 18.

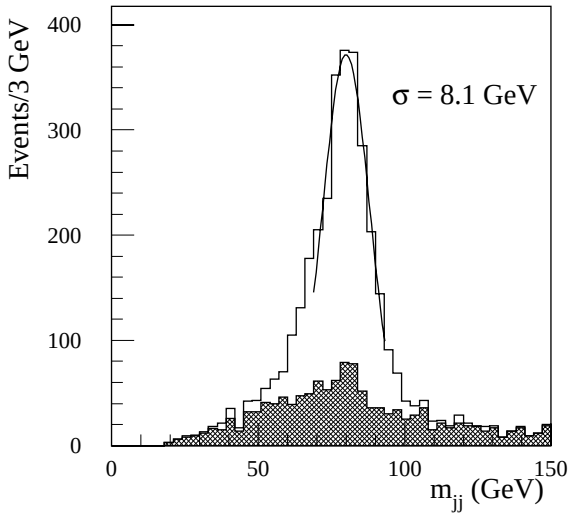

Figure 9-61 Invariant mass distribution of the accepted *jj* pairs from the fully-simulated inclusive $t\bar{t}$ sample (see text). The shaded histogram shows the background from wrong combinations.

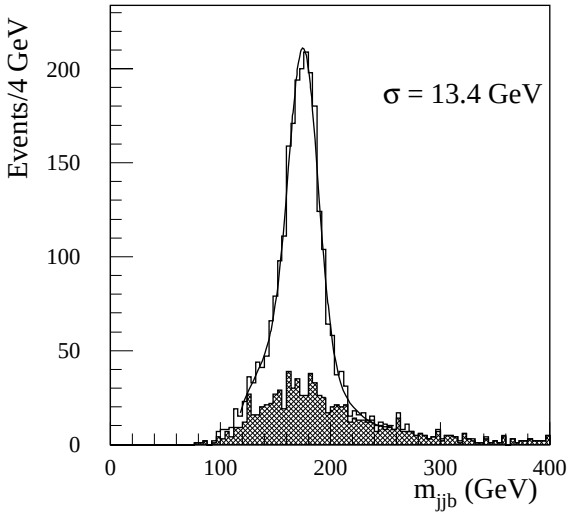

Figure 9-62 Invariant mass distribution of the accepted *jjb* combinations from the fully-simulated inclusive $t\bar{t}$ sample (see text). The shaded histogram shows the background from wrong combinations.

9.3.4.2 $t\bar{t}H$ with $H \rightarrow b\bar{b}$

Production of $t\bar{t}H$, followed by $H \rightarrow b\bar{b}$, is a promising channel to search for a Higgs boson decaying hadronically in the mass range around 100 GeV, both in the framework of the Standard Model and of the MSSM (Chapter 19). A high-statistics sample of fully-simulated $t\bar{t}H$ events, with $H \rightarrow b\bar{b}$, was used to assess the capability of reconstructing these final states [9-25]. Electronic noise and pile-up were not included. One top was required to decay semileptonically and the other one hadronically. Since there are four *b*-jets in the final state, combinatorial background from wrong jet pairings is potentially very large in this channel. To overcome this problem, both top quarks were reconstructed. Firstly, only combinations of pairs of light-quark jets which are compatible with coming from $W \rightarrow jj$ decays were selected by requiring $m_{jj} = m_W \pm 25$ GeV. The jet four-momenta were scaled by imposing that the reconstructed *jj* mass be equal to the nominal *W* mass. The lepton momentum and the E_T^{miss} vector where used to reconstruct the decay $W \rightarrow l\nu$ (with a twofold ambiguity on the neutrino longitudinal momentum). Then, the accepted di-jet pairs and the $l\nu$ pair where combined with *b*-jets and the pairing which minimised $\chi^2 = (m_{jjb} - m_t)^2 + (m_{l\nu b} - m_t)^2$ was chosen. The resulting $t \rightarrow jjb$ mass spectrum is shown in Figure 9-63. The mass resolution is about 12 GeV, and 75% of the events are contained in a $\pm 2\sigma_m$ mass window centred on the peak. After both top quarks were recon-

structed, the invariant mass distribution of the two remaining *b*-jets showed a peak from $H \rightarrow b\bar{b}$ decays (Figure 9-64). The mass resolution is about 20 GeV and the acceptance in a $\pm 2\sigma_m$ mass window 63%. The fraction of events where both *b*-jets come from the Higgs decay is about 60% (shaded distribution in Figure 9-64).

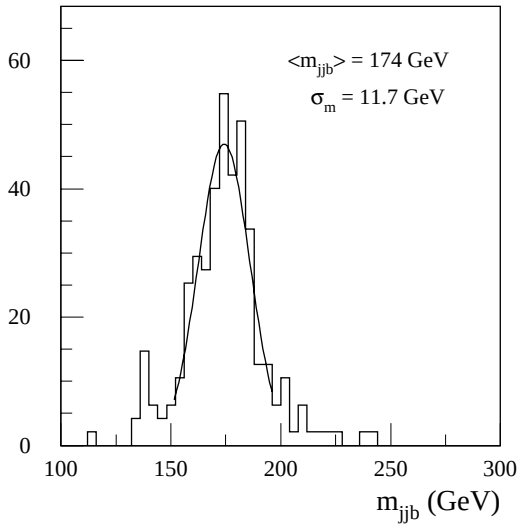

Figure 9-63 Reconstructed top mass from the decay $t \rightarrow jjb$ in $\bar{t}tH$ events.

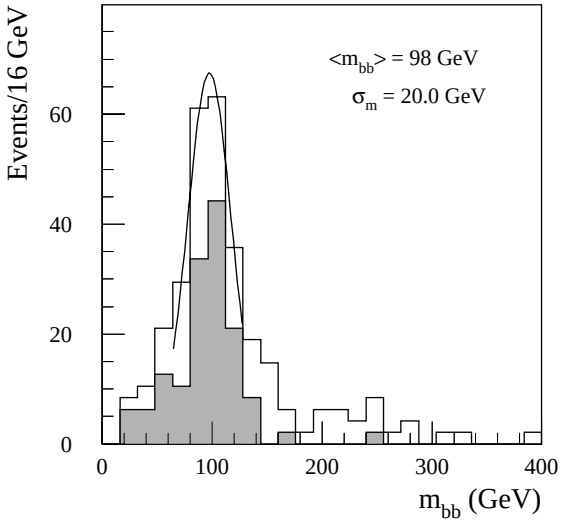

Figure 9-64 Reconstructed $H \rightarrow b\bar{b}$ mass spectrum in $\bar{t}tH$ events, as obtained after reconstructing both top quarks. The shaded distribution is for events where both *b*-jets come from the Higgs decay.

9.4 Conclusions

The main aspects of the measurement of jets, τ's and missing transverse momentum, as well as the reconstruction of the masses of objects decaying to jets or τ's have been discussed in this chapter. The performance of the ATLAS calorimetry for the reconstruction of jets has been studied. The calorimeters are non-compensating and an algorithm for jet energy reconstruction is applied that corrects for this effect and adds correction terms for the energy loss in the dead material. The intrinsic performance of the detector, in the precision region that extends up to $|\eta| = 3$, is of the order of, or better, than $\sigma/E = 50\%/\sqrt{E} \oplus 3\%$, the target resolution to fulfil the physics goals. The resolution degrades when the jet reconstruction is limited to a cone or when the jet points to a crack region. The coefficients of the energy reconstruction algorithm can be parametrised as smooth functions of the jet energy. Residual non-linearities are of the order of 2 to 3% for jet energies in the range 20 to 1000 GeV. Effects of the order of a few percents that may affect the extrapolation of the calibration to very high-p_T have been briefly discussed. The influence of the jet algorithm and the effect of minimum-bias events on the relation between the reconstructed jet energy and the parton energy has been illustrated in a few physics examples.

Low-p_T jets have been investigated. At low luminosity, the jet veto threshold can be lowered to 15 GeV, while at high luminosity, to maintain a good efficiency for the signal, it has to be raised to 25 GeV. The performance for forward jet tagging in the pseudorapidity range $2 < |\eta| < 5$ has been presented. A tagging efficiency of 90% is obtained up to $|\eta| = 4.0$, then it decreases to about 50% at $|\eta| = 4.8$. At high luminosity, efficiencies of 80% can be obtained with a fake jet rate not higher than 10%.

Hadronic τ decays can be efficiently reconstructed and identified by using the information from the calorimeters and the Inner Detector. For a τ identification efficiency of ~20%, a rejection factor of 170 to 1200 can be achieved against jets from W+jets and $t\bar{t}$ production and of about 1700 against b-jets. This performance, which is similar at low and high luminosity, allows good sensitivity to the $A \rightarrow \tau\tau$ channel in the mass range 100 to 500 GeV (Chapter 19).

The most relevant issues for a good performance in E_T^{miss} measurement have been reviewed: the calorimeter calibration and coverage, and the cuts applied when summing cell energies in presence of electronic noise and pile-up from minimum bias events. At low luminosity, the resolution is well fitted by the form $\sigma(p_{xy}^{miss}) = 0.46 \times \sqrt{\Sigma E_T}$. At high luminosity, the E_T^{miss} resolution degrades by about a factor two. Tails in the E_T^{miss} distribution have been investigated. No large tails are being produced when a high-p_T jet points to a less uniform region of the calorimeter but some degradation of the resolution is observed.

Various cases of mass reconstruction have been investigated: $W \rightarrow jj$, $H \rightarrow b\bar{b}$, $Z \rightarrow \tau\tau$ and $H/A \rightarrow \tau\tau$, and $t\bar{t}$ final states. The typical mass resolution for W bosons of p_T = 100–200 GeV is 8 GeV at low luminosity and 13 GeV at high luminosity. For W bosons of several hundred GeV p_T, systematic effects arise from the overlap between the two jets. The mass resolution for a Higgs boson of mass 100 GeV decaying into $b\bar{b}$ pairs is about 15 GeV both at high and low luminosity, whereas the mass resolution for resonances decaying to τ pairs ($Z/H/A \rightarrow \tau\tau$) is typically 10% at low luminosity. At high luminosity, the degradation of the E_T^{miss} resolution due to the pile-up affects significantly (factor ~2) the width of the reconstructed $\tau\tau$ spectra. Finally, events containing top-quark pairs can be efficiently reconstructed, with a mass resolution for fully hadronic top decays of about 13 GeV. In some cases (*e.g.* $t\bar{t}H$ production), the presence of top quarks in the final state can be used to extract a signal from new physics over the background.

9.5 References

9-1 J. Sjölin, 'Jet reconstruction in the ATLAS Barrel Calorimeter', ATLAS Internal Note ATL-COM-TILECAL-99-012 (1999).

9-2 ATLAS Collaboration, Calorimeter Performance Technical Design Report, CERN / LHCC / 97-1 (1997).

9-3 A. Kiryunin *et al.*, 'Jet energy measurement in the End-Cap region', ATLAS-HEC-047 (1998).

9-4 M. Cobal *et al.*, 'Analysis results of the first combined test of the LArgon and TILECAL barrel calorimeter prototypes', ATLAS Internal Note ATL-TILECAL-95-067 (1995).

9-5 F. Ariztizabal *et al.*, 'Construction and performance of an iron-scintillator hadron calorimeter with longitudinal tile configuration', Nucl. Instr. Meth. **A349** (1994) 384.

9-6 M.P. Casado and M. Cavalli-Sforza, 'H1-inspired analysis of the 1994 combined test of the Liquid Argon and Tile Calorimeter', ATLAS Internal Note ATL-TILECAL-96-075 (1996).

9-7 M. Cobal *et al.*, 'Analysis results of the April 1996 combined test of the LArgon and TILECAL barrel calorimeter prototypes', ATLAS Internal Note ATL-TILECAL-98-168 (1998).

9-8 R. Lefevre and C. Santoni, 'A study of jet energy reconstruction', ATLAS Internal Note ATL-COM-PHYS-99-041 (1999).

9-9 W. Braunschweig *et al.* (*H1* calorimeter group), Nucl. Instr. Meth. **A265** (1988) 246, DESY 89-022 (1989), and B. Andrieu *et al.* (*H1* calorimeter group), DESY 93-04 (1993).

9-10 M. Bosman *et al.*, 'Jet Finder Library: version 1.0', ATLAS Internal Note ATL-SOFT-98-038 (1998).

9-11 I. Efthymiopoulos, 'Comparison between the ATLAS/Tilecal hadron Barrel Calorimeter prototype test beam data and Hadronic Simulation packages', ATLAS Internal Note ATL-TILECAL-96-092 (1996), Frascati Physics Series Vol. VI (pp.497-507), VI Int. Conf. on Calorimetry in HEP, Frascati, June 8-14 1996.

9-12 M. Bosman *et al.*, 'Conclusions of the workshop on ATLAS requirements on shower models', ATLAS Internal Note ATL-COM-PHYS-99-056 (1999).

9-13 T.A. Gabriel *et al.*, 'Energy dependence of hadronic activity', Nucl. Instr. Meth. **A338** 336 (1994).

9-14 H. Seymour, Z. Phys. **C62** 127 (1993).

9-15 I.C. Park, 'A new Clustering Algorithm: Mulguisin', ATLAS Internal Note ATL-COM-PHYS-99-055 (1999).

9-16 V. Cavasinni *et al.*, 'Search for $H \rightarrow WW \rightarrow l\nu jj$ with the ATLAS Detector (m_H = 300-600 GeV)', ATLAS Internal Note ATL-PHYS-98-127 (1998).

9-17 P. Savard and G. Azuelos, 'The discovery potential of a Heavy Higgs (m_H > 800 GeV) using full GEANT simulation of the ATLAS detector', ATLAS Internal Note ATL-PHYS-98-007 (1998).

9-18 D. Cavalli *et al.*, 'Search for $A/H \rightarrow \tau\tau$ decays', ATLAS Internal Note ATL-PHYS-94-051 (1994).

9-19 D. Cavalli and S. Resconi, 'Tau-jet separation with the ATLAS detector', ATLAS Internal Note ATL-PHYS-98-118 (1998).

9-20 ATLAS Collaboration, Inner Detector Technical Design Report, CERN/LHCC 97-16 (1997).

9-21 E. Richter-Was, D. Froidevaux and L. Poggioli, 'ATLFAST 2.0 a fast simulation package for ATLAS', ATLAS Internal Note ATL-PHYS-98-131 (1998).

9-22 D. Cavalli, 'Missing transverse momentum reconstruction in ATLAS', ATLAS Internal Note ATL-PHYS-96-080 (1996).

9-23 P. Savard, 'The *W* to jet-jet and top mass reconstructions with the ATLAS Detectors', ATLAS Internal Note ATL-CALO-97-092 (1997).

9-24 D. Cavalli and S. Resconi, 'Comparison between full simulation and fast simulation of the ATLAS detector', ATLAS Internal Note ATL-PHYS-97-100 (1997).

9-25 D. Cavalli and M. Sapinski, 'Full and fast simulation and reconstruction of Higgs decay channels with multi-*b*-jets final states', ATLAS Internal Note ATL-PHYS-99-033 (1999).

9-26 Y. Coadou *et al.*, 'Identification of hadronic tau decays in ATLAS', ATLAS Internal Note ATL-PHYS-98-126 (1998).

9-27 S. Wasserbaech, ‘Review of tau lifetime measurements’, Tau ’98, Fifth International Workshop on Tau Lepton Physics, Santander, Spain (1998).

9-28 S. Haywood, ‘Offline calibration and alignment of the Inner Detector’, ATLAS Internal Note ATL-INDET-99-001 (1999).